Article

Immunity

Targeting immune cells in the aged brain reveals that engineered cytokine IL-10 enhances neurogenesis and improves cognition

Graphical abstract

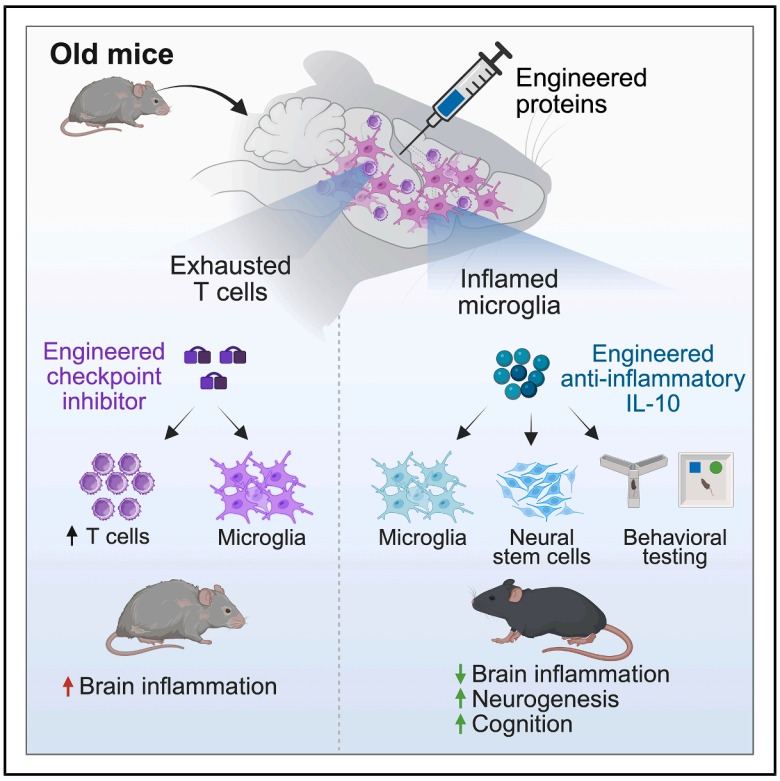

Authors

Paloma Navarro Negredo, Justin You, Max Hauptschein, ..., Saul A. Villeda, K. Christopher Garcia, Anne Brunet

Correspondence

paloma.navarro@epfl.ch (P.N.N.), abrunet1@stanford.edu (A.B.)

In brief

Immune cells populate the old brain, but whether they can be specifically targeted to improve brain function in older individuals remains unclear. Navarro Negredo et al. dissect how aging impacts brain immune activity and show that targeting immune cells with an engineered IL-10 variant rebalances inflammatory programs in microglia, improves neurogenesis, and enhances cognition in old mice.

Highlights

- The old brain contains exhausted T cells and unbalanced microglial inflammation
- Delivery of engineered proteins into old mouse brains allows immune cell targeting
- Checkpoint inhibition in old brains activates T cells and microglial inflammation
- Engineered IL-10 restores microglial balance, neurogenesis, and cognition in old mice

Navarro Negredo et al., 2026, Immunity *59*, 458–476
February 10, 2026
https://doi.org/10.1016/j.immuni.2026.01.016

CellPress

CellPress
OPEN ACCESS

Immunity

Article

Targeting immune cells in the aged brain reveals that engineered cytokine IL-10 enhances neurogenesis and improves cognition

Paloma Navarro Negredo,[1,13,*] Justin You,[1,12] Max Hauptschein,[1,12] Adam B. Schroer,[2,12] Daniel J. Richard,[1] Gita C. Abhiraman,[3,4] Andy P. Tsai,[5,6] Eric D. Sun,[1] Giulia Notarangelo,[1] Julliana Ramirez-Matias,[1] Olivia Y. Zhou,[1,4] Matthew T. Buckley,[1] Karen E. Malacon,[1,4] Lucy Xu,[1] Juliana Sucharov,[2] Eduardo Ramirez Lopez,[5,6] Lora Picton,[3] Tony Wyss-Coray,[5,6] Robert A. Saxton,[3,14] Ricardo A. Fernandes,[3,15] Saul A. Villeda,[2,7,8] K. Christopher Garcia,[3,5,9,10] and Anne Brunet[1,5,6,11,16,*]

[1]Department of Genetics, Stanford University, Stanford, CA, USA
[2]Department of Anatomy, University of California, San Francisco, San Francisco, CA, USA
[3]Department of Molecular and Cellular Physiology, Stanford University School of Medicine, Stanford, CA 94305, USA
[4]Stanford Medical Scientist Training Program, Stanford University, Stanford, CA, USA
[5]Phil and Penny Knight Initiative for Brain Resilience, Stanford University, Stanford, CA, USA
[6]Wu Tsai Neurosciences Institute, Stanford University, Stanford, CA, USA
[7]Department of Physical Therapy and Rehabilitation Science, University of California, San Francisco, San Francisco, CA, USA
[8]Bakar Aging Research Institute, University of California, San Francisco, San Francisco, CA, USA
[9]Department of Structural Biology, Stanford University School of Medicine, Stanford, CA, USA
[10]Howard Hughes Medical Institute, Stanford University School of Medicine, Stanford, CA, USA
[11]Glenn Center for the Biology of Aging, Stanford University, Stanford, CA, USA
[12]These authors contributed equally
[13]Present address: Global Health Institute, Swiss Federal Institute of Technology Lausanne (EPFL), Lausanne, Switzerland
[14]Present address: Department of Molecular and Cell Biology, University of California at Berkeley, Berkeley, CA, USA
[15]Present address: Chinese Academy of Medical Sciences Oxford Institute, University of Oxford, Oxford, UK
[16]Lead contact
*Correspondence: paloma.navarro@epfl.ch (P.N.N.), abrunet1@stanford.edu (A.B.)
https://doi.org/10.1016/j.immuni.2026.01.016

SUMMARY

The immune system could play an important role in the age-related decline in brain function, yet specific immune-based strategies to enhance brain resilience in older individuals are lacking. Here, we combined engineered proteins and direct brain delivery to target immune cell populations within the old brain. We detected T cells with an exhaustion signature in the old brain and targeted them with a potent engineered checkpoint inhibitor (RIPR-PD1). This led to T cell expansion and strong pro-inflammatory responses in many brain cell types, notably microglia. To rescue age-related inflammatory imbalances in microglia, we used the anti-inflammatory cytokine interleukin (IL)-10. IL-10 boosted anti-inflammatory responses in old microglia, but it also triggered pro-inflammatory signaling. An engineered IL-10 variant that uncouples pro- and anti-inflammatory responses positively impacted the transcriptome of multiple cell types, enhanced neurogenesis, and improved cognition in aged mice. Our findings pave the way for immunotherapies for the aged brain.

INTRODUCTION

Brain function deteriorates with age. Additionally, age-related neurodegenerative diseases (e.g., Alzheimer's disease and Parkinson's disease) surge in the elderly population. While many pathways are remodeled in the brain during aging,[1–4] a key feature of old brains is immune cell infiltration and inflammation. Aging leads to a pronounced increase in the number of T cells across several brain regions in mice and humans,[5–7] including neural stem cell (NSC) niches[8–11] and white matter tracts.[12–16] T cells from old brains are clonally expanded,[8,17] suggesting they have encountered antigens. T cell infiltration and clonal expansion are further accentuated in age-related neurodegenerative diseases.[18–26] In parallel, pro-inflammatory pathways are strongly upregulated during aging in many cell types, and this is exacerbated in Alzheimer's disease.[8,13,27–36] A systematic understanding of age-related changes in brain immune cells may inform strategies to mitigate brain aging.

Could immune-based interventions be designed to counter brain aging? Modulating immune cells and inflammatory pathways can affect the old brain.[12,13,28,30,37–39] But previous studies have relied on broad interventions, often performed in the

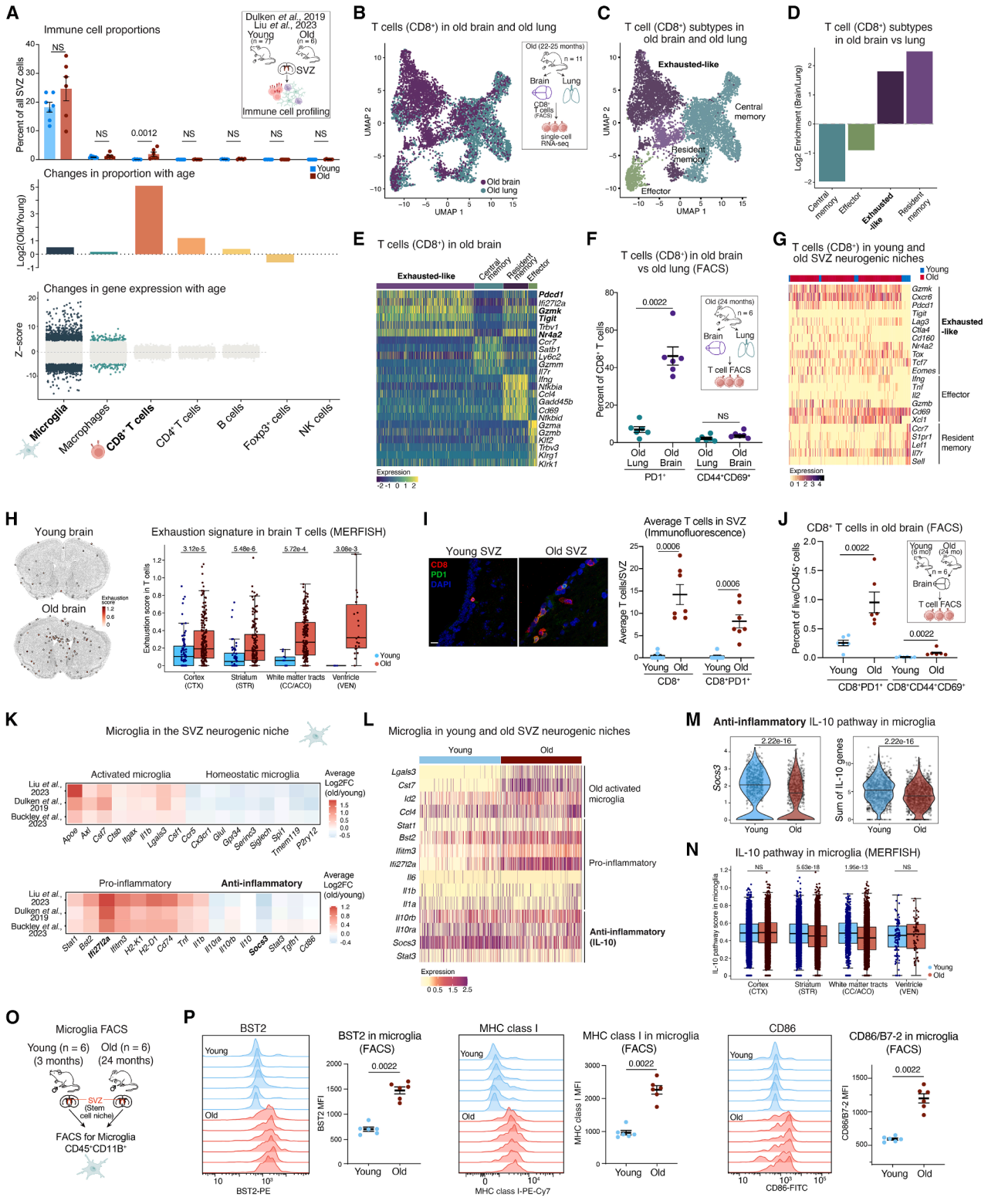

Figure 1. Characterization of immune cells in the old brain

(A) Analysis of immune cell populations in the SVZ neurogenic niche of young (3–4 months, $n = 7$) and old (22–29 months, $n = 6$) male mice in two merged scRNA-seq published datasets.[8,50] Top panel, quantification of the proportion of different immune cell types relative to the total number of cells. Data are mean ± SEM; each dot represents one mouse. Middle panel, age-dependent changes ($\log_2$[old/young]) in the abundance of each cell type. Bottom panel, age-dependent

(legend continued on next page)

periphery[13] and in young or disease model mice.[18,24,40–45] We lack strategies to target specific immune cell subsets and pathways within the old brain to determine their mode of action. Moreover, identifying such brain immune interventions could help develop "aging immunotherapies" and would be critical to counter aspects of brain aging and age-related brain diseases.

Here, we developed a platform that leverages engineered proteins and direct brain delivery to test immune cell-specific interventions in old mice. We identified T cells with an exhaustion signature and targeted them with a potent engineered checkpoint inhibitor, leading to T cell expansion and strong pro-inflammatory responses in many cell types, including microglia. To rescue age-related inflammatory balance in microglia, we used an engineered interleukin (IL)-10 variant that uncouples pro- and anti-inflammatory responses and found that it had beneficial effects on multiple cell types and cognition in aged mice. Our findings pave the way for novel immunotherapies for the aged brain.

RESULTS

Characterization of immune cells in the aged brain

We systematically characterized immune cells in the aging brain, focusing on the subventricular zone (SVZ) neurogenic niche—a region that contains adult NSCs and declines during aging.[46–49] Leveraging previously published single-cell RNA-sequencing (scRNA-seq) datasets,[8,50] we found that SVZ neurogenic niches contained microglia (the brain-resident myeloid population), macrophages, CD8$^+$ T cells, CD4$^+$ T cells, and low numbers of other immune cells (Figures 1A and S1A). CD8$^+$ T cells were not very numerous but significantly increased in number with age (Figure 1A, upper and middle panel). Microglia were the most abundant immune cell type and showed the largest age-related changes in gene expression (Figure 1A, lower panel). We thus focused on CD8$^+$ T cells and microglia for further characterization and targeting in the old brain.

CD8$^+$ T cells with an exhaustion signature increase in the aging brain

We generated an scRNA-seq dataset of CD8$^+$ T cells (3,724 cells) freshly isolated from brains of old male mice (22–25 months, n = 11 mice, pooled). For comparison, we isolated CD8$^+$ T cells (4,976 cells) from a peripheral organ (lung) of the same old mice (Table S1). Clustering showed that CD8$^+$ T cells were different in old brains and old lungs (Figure 1B) and encompassed four main T cell subtypes: central memory, effector/activated, resident memory, and exhausted-like (Figures 1C, S1B, and S1C; Table S1). In old brains, exhausted-like T cells were more prevalent than in old lungs and scored higher for "exhaustion" signatures (Figures 1D and S1D). We validated that CD8$^+$ T cells positive for the checkpoint protein PD1 (an exhaustion marker) were more abundant in old brains than in old lungs, by using fluorescence-activated cell sorting (FACS) (Figure 1F). Effector/memory CD8$^+$ T cells (CD44$^+$CD69$^+$) were less prevalent and not significantly different between old brains and old lungs (Figure 1F).

CD8$^+$ T cells in old brains and old neurogenic niches expressed multiple markers of exhaustion, including checkpoint protein genes (*Pdcd1*, *Tigit*, and *Ctla4*), transcription factors (*Tox* and *Nr42a*), and the age-associated gene *Gzmk* (Figures 1E, 1G, and S1E). This profile has been reported in other tissues

changes in gene expression per cell type. Dots represent differential expression MAST Z score for each gene. Genes significantly changed with age (Bonferroni-corrected $p < 0.05$) are in color.
(B) scRNA-seq analysis of CD8$^+$ T cells freshly isolated from the brain and lung of old male mice (22–25 months, n = 11 mice, pooled). Uniform manifold approximation and projection (UMAP) clustering of all T cells colored by organ of origin, downsampled to 3,724 cells per organ. One independent experiment.
(C) UMAP as in (B) colored by cell type.
(D) Changes in the percentage of T cell subtypes in old brains vs. old lungs.
(E) Heatmap of top six marker genes for each T cell subtype in the old brain.
(F) FACS quantification of percent PD1$^+$ and CD44$^+$CD69$^+$ of CD8$^+$ T cells freshly isolated from the brains and lungs of old male mice (24 months, n = 6). One independent experiment.
(G) Heatmap of T cell marker genes in T cells from same dataset as (A).
(H) Left, representative images showing exhaustion scores for T cells in coronal brain sections of young (6 months) and old (28 months) male mice in a spatial transcriptomics (MERFISH) dataset.[7] Right, quantification of exhaustion scores in T cells from young (3–6 months, n = 5) and old (26–34 months, n = 6) male mice across four brain regions, cortex (CTX), striatum and adjacent regions (STR), white matter tracts of the corpus callosum and anterior commissure (CC/ACO), and the ventricle (VEN). One coronal section per mouse. Boxplots of median and lower and upper quartile values.
(I) Left, representative immunofluorescence images of SVZ from young (4 months) and old (28 months) male mice. Red, CD8$^+$ (T cells); green, PD1$^+$ (checkpoint protein); blue, DAPI (nuclei). Scale bar, 10 μm. Right, number of CD8$^+$ and CD8$^+$ PD1$^+$ T cells in the SVZ of young (3–4 months, n = 7) and old (28–32 months, n = 7) male mice. Each dot represents one mouse (average of two sections per mouse). One independent experiment.
(J) FACS quantification of the percentage of CD8$^+$PD1$^+$ and CD8$^+$CD44$^+$CD69$^+$ T cells of live/CD45$^+$ cells freshly isolated from the brain of young (6 months, n = 6) and old (24 months, n = 6) male mice. One independent experiment.
(K) Average changes in gene expression in microglia of the SVZ neurogenic niche of young and old male mice from three published scRNA-seq datasets.[8,50,51] Red, upregulated; blue, downregulated genes.
(L) Heatmap of log-normalized counts for pro- and anti-inflammatory genes in microglia from the SVZ in a published dataset.[8]
(M) Log-normalized expression values of *Socs3* (left) and combined genes in the IL-10 pathway in microglia from the SVZ in a published dataset.[8] Horizontal lines, median.
(N) IL-10 signaling scores for microglia in spatial transcriptomics dataset.[7]
(O and P) FACS histograms and quantification of inflammation proteins in microglia (CD45$^+$CD11b$^+$) freshly isolated from the SVZ of young (3 months) and old (24 months) male mice (n = 6). Each dot represents one mouse (mean fluorescence intensity [MFI] values from ~500 microglia per mouse). One independent experiment.
Data are mean ± SEM. p values, two-sided Wilcoxon rank-sum test. NS, not significant.
See also Figure S1.

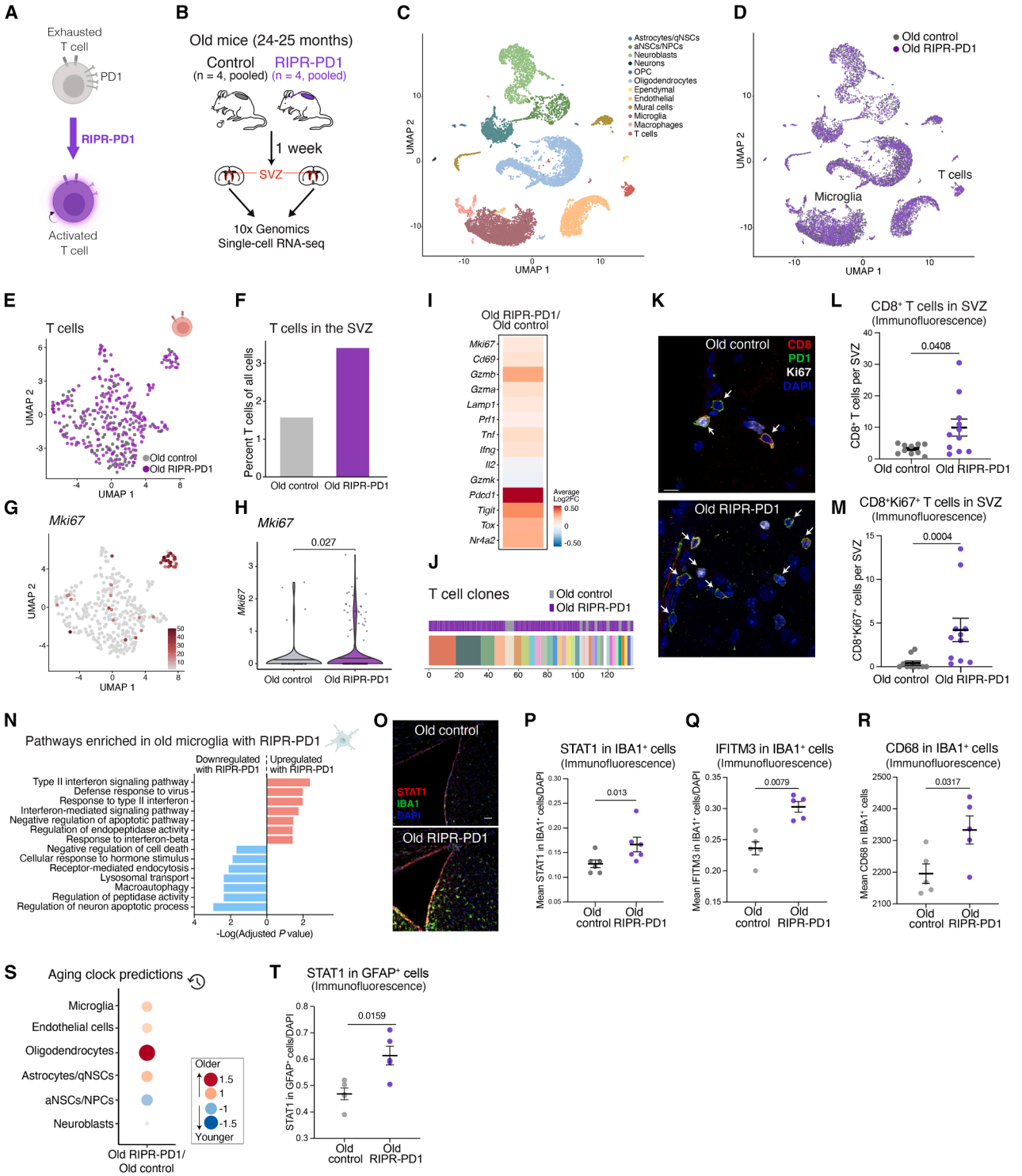

Figure 2. Targeting exhausted T cells in the old brain with an engineered checkpoint inhibitor

(A) RIPR-PD1 is engineered to potently inhibit checkpoint (PD1) signaling and drive T cells to an activated state.[68]

(B) Old male mice (24–25 months) were infused with mouse RIPR-PD1 or control (5 mg/mL, *n* = 4 mice per condition, pooled) for 1 week, by stereotaxic implantation of mini-osmotic pumps into the lateral ventricle of the brain (adjacent to the SVZ). Brains were perfused with PBS to remove blood, SVZ neurogenic niches dissociated, and SVZs from the same conditions pooled and briefly FACS-sorted to remove debris. scRNA-seq was performed on the entire SVZ (10× Genomics), followed by sequencing (Illumina Next-seq). For independent experiment, see Figure S3.

(C) UMAP clustering colored by cell type, downsampled to 6,236 cells per condition. Abbreviations, quiescent neural stem cells, qNSCs; activated neural stem cells, aNSCs; neural progenitor cells, NPCs; oligodendrocyte progenitor cells, OPCs.

(legend continued on next page)

and blood of old mice and humans.[52,53] These T cells accumulated in old neurogenic niches but were rare in young niches (Figures 1G, S1E, and S1F). Importantly, re-analysis of our longitudinal spatial transcriptomics (MERFISH) dataset[7] confirmed that T cell exhaustion signatures increased with age across multiple brain regions (Figure 1H). T cell memory scores decreased in several regions (Figure S1G) and effector scores remained unchanged. Hence, exhausted-like T cells increased throughout the brain during aging (although their origin was not clear).

Using immunostaining, we validated the increase in $CD8^+$ $PD1^+$ T cells in the SVZ of old mice compared with young mice (Figure 1I). In fact, in old mice, ~50% of $CD8^+$ T cells also expressed PD1 (Figure S1H). Similarly, we observed a significant increase in the number of $CD8^+PD1^+$ (and $CD8^+CD44^+CD69^+$) T cells in old brains, compared with young brains, by FACS (Figure 1J), although the percentage of $CD8^+$ T cells that were $PD1^+$ were similar in young and old brains (Figure S1I). Thus, the old brain contains many T cells with an exhaustion signature, which could be leveraged for interventions.

Inflammatory pathways increase and anti-inflammatory pathways decrease in aged microglia

Supporting previous findings,[8,9,13,16,27,32,35,42,53-57] we found that old microglia of the SVZ[8,50,58] exhibited a pro-inflammatory, activated phenotype with higher expression of interferon (IFN)-stimulated genes and pro-inflammatory cytokines (Figures 1K, 1L, and S1J–S1L; Table S2). We confirmed elevated pro-inflammatory IFN signaling in old microglia in our spatial transcriptomics dataset[7] (Figure S1M). However, how anti-inflammatory pathways change in microglia with aging remains largely unexplored. Microglia of the old SVZ only showed detectable expression of the anti-inflammatory cytokine receptors IL-10 and transforming growth factor beta (TGF-β) (see Figure S4A). Old microglia exhibited a downregulation of genes in the anti-inflammatory IL-10 response pathway, compared with young microglia (Figures 1K–1M and S1J–S1L), which was also observed in our spatial transcriptomics dataset[7] (Figure 1N). We experimentally validated these changes by assessing protein expression using FACS (Figure 1O). Microglia from the old SVZ exhibited higher IFN -induced proteins MHC class I and BST2 (Figure 1P) and the costimulatory protein CD86/B7-2 (which is normally suppressed by IL-10[59–61]) (Figure 1P). Thus, aged microglia showed not only an increase in pro-inflammatory pathways but also a decrease in anti-inflammatory signaling pathways, which could be targeted for interventions.

Our systematic analysis revealed two main immune-related changes in old brains: an increase in T cell number, dominated by a population of $CD8^+$ T cells with exhaustion signatures; and an imbalance in pro-inflammatory and anti-inflammatory signaling pathways in microglia. We built a platform leveraging engineered proteins and direct brain delivery to test the effects of precisely targeting these immune cell signatures in old brains.

T cells in old brains can be targeted directly with checkpoint inhibitors

The effects of targeting exhausted T cells directly and exclusively in the old brain remain largely unexplored. T cells expressing checkpoint proteins (e.g., PD1) can be activated with checkpoint inhibitors, widely used in cancer.[62–67] We used an engineered protein, "receptor inhibition by phosphatase recruitment to PD1" (RIPR-PD1), to potently inhibit the checkpoint protein PD1[68] (Figure 2A). We directly delivered RIPR-PD1 into the brain of old mice by implanting mini-osmotic pumps stereotaxically in the lateral ventricle, adjacent to the SVZ.[28,69–74] We verified by FACS that RIPR-PD1 was more potent than classical anti-PD1 antibodies at increasing the number of $CD8^+$ T cells in the old SVZ (Figures S2A and S2B) and did so in a dose-dependent manner (Figures S2C and S2D). To unbiasedly test the impact of RIPR-PD1 on different cell types in the old neurogenic niche, we continuously infused mouse RIPR-PD1 (hereafter RIPR-PD1) or control (human RIPR-PD1, unable to bind to mouse PD1[68]) into the brain of old mice (24–25 months, $n = 4$ male mice per condition, pooled) and performed scRNA-seq on the entire SVZ after 1 week (Figure 2B, experiment #1; Table S1). Importantly, we replicated our findings in an independent scRNA-seq experiment (Figure S3L, experiment #2; Table S1). We

(D) Same as (C), colored by condition.
(E) UMAP clustering of T cells from the SVZ colored by condition (control, 98 T cells; RIPR-PD1, 244 T cells).
(F) Percentage of T cells out of all cells per condition.
(G and H) UMAP (G) and violin plot (H) showing log-normalized expression values for *Mki67* in T cells. Darker red color indicates higher expression. Horizontal lines, median.
(I) Heatmap of average $\log_2$ fold change in expression of T cell marker genes in RIPR-PD1 vs. control T cells. Red, upregulated; blue, downregulated genes in RIPR-PD1.
(J) Clonality of T cells by TCR sequencing. Bottom row, TCR-β sequence clones arranged in order of decreasing frequency. Top row, source of the T cells.
(K–M) Representative immunofluorescence images (K) and quantification of $CD8^+$ T cells (L) and $CD8^+Ki67^+$ T cells (M) in the SVZ from old male mice (24–26 months) infused with control or RIPR-PD1 (n = 10–11 male mice per condition, combined over two independent experiments). Red, CD8 (T cells); green, PD1 (checkpoint protein); white, Ki67 (proliferating cells); blue, DAPI. Scale bar, 10 μm. Each dot represents one mouse (average of three coronal sections per mouse).
(N) Gene Ontology (GO) biological processes pathways enriched in microglia from old male mice treated with RIPR-PD1 vs. control. For all pathways shown, false discovery rate (FDR) < 0.05, EnrichR statistics. See Table S2.
(O and P) Representative immunofluorescence images (O) and quantification (P) of STAT1 fluorescence intensity overlapping with IBA1 in SVZ of old male mice (24–26 months) treated with control or RIPR-PD1 (n = 6). Red, STAT1 (IFN response); green, IBA1 (microglia); blue, DAPI. Scale bar, 50 μm. Each dot represents one mouse (average of three coronal sections per mouse). Representative of two independent experiments.
(Q and R) Same as (O) but for IFITM3 (Q) or CD68 (R) in a different cohort of old male mice (24 months, n = 5).
(S) Effect sizes summarize the difference in median predicted ages between old RIPR-PD1 and old control for each cell type calculated by aging clocks.[51] Red, increase in predicted age (pro-aging); blue, decrease in predicted age (pro-rejuvenating).
(T) Quantification of STAT1 fluorescence intensity overlapping with astrocyte/NSC cell marker (GFAP) fluorescence as in (Q).
Data are mean ± SEM. p values, two-sided Wilcoxon rank-sum test.
See also Figures S2 and S3.

identified 12 distinct cell types in the old neurogenic niche, including cells of the neural lineage; endothelial cells; and immune cells like microglia, macrophages, and T cells (Figures 2C, 2D, S3A, S3M, and S3N; Table S1)—as previously observed.[8,50,58,75]

RIPR-PD1 increases the T cell population and microglial inflammation in old brains

We analyzed the effects of RIPR-PD1 on immune cells. RIPR-PD1 led to an increase in the proportion of T cells in the old SVZ neurogenic niche (Figures 2E, 2F, S3B, S3C, S3O, and S3P), including T cells expressing the proliferation marker *Mki67* (Figures 2G–2I and S3Q–S3S), suggesting that proliferation could account for the increase in T cell number. T cell receptor (TCR) sequencing showed more clonally expanded T cells in the SVZ of old mice treated with RIPR-PD1 (Figures 2J and S3T), indicating antigen-dependent T cell activation. T cells showed a trending increase in some activation markers (*Cd69*, *Gzmb*, and *Gzma*) and a significant increase in *Tnf*, *Pdcd1*, and *Tigit* (Figures 2I, S3D, and S3S), as well as an increase in exhaustion genes and signatures (Figures 2I, S3E, S3F, and S3S). The increase in exhaustion markers could be due to T cell activation combined with the continuous presence of antigens and PD1 ligand (PD-L1) in the niche (Figure S3G) and compensatory mechanisms in T cells.[62,66] Using immunostaining, we validated that RIPR-PD1 led to the expansion of $CD8^+$ T cells, as well as proliferating T cells ($CD8^+Ki67^+$ and $CD8^+Ki67^+PD1^+$) in the old SVZ (Figures 2K–2M, S2E, and S2F). Thus, direct delivery of the engineered checkpoint inhibitor RIPR-PD1 expanded the population of T cells in the old brain.

In parallel, microglia of the old SVZ showed an upregulation of response to type II IFN (IFN-γ) genes with RIPR-PD1 (Figures 2N and S3U; Table S2). Immunostaining confirmed a strong increase in STAT1 and IFITM3 (IFN-induced proteins) in microglia (labeled with IBA1 or TMEM119) of the old SVZ infused with RIPR-PD1 (Figures 2O–2Q, S2G, and S2H). We further validated microglial inflammation by using FACS (Figure S2I). We also observed an increase in the microglial activation marker CD68/macrosialin (Figure 2R). To test whether RIPR-PD1 might act directly on microglia (which also expressed PD1 and CD45 [Figures S3H and S3I]), we incubated primary microglia with control or RIPR-PD1 *in vitro* and assessed IFN-induced proteins by FACS. Under these conditions, RIPR-PD1 did not induce IFN signaling on microglia (Figure S2J). Our results suggest that the inflammatory effects of RIPR-PD1 on microglia are likely due to RIPR-PD1's ability to activate T cells (although we cannot exclude that RIPR-PD1 may act directly on microglia or indirectly through other cell types *in vivo*).

RIPR-PD1 has "pro-aging" effects on many cell types of the old neurogenic niche

To unbiasedly assess the impact of RIPR-PD1 on other cell types of the old neurogenic niche, we used our cell-type-specific "aging clocks," which can estimate the age of different cell types and quantify transcriptomic rejuvenation in the SVZ.[51] Mirroring the strong increase in pro-inflammatory signaling, aging clocks predicted RIPR-PD1 to have a pro-aging effect on microglia (Figures 2S, S3K and S3V). In contrast, RIPR-PD1 had a small pro-rejuvenating effect on activated NSCs (aNSCs)/neural progenitor cells (NPCs) (Figures 2S, S3K, and S3V), consistent with enrichment for cell proliferation genes (Figure S3J; Table S3). Experimentally, however, RIPR-PD1 infusion was not sufficient to increase the generation of new neurons (neurogenesis) in the SVZ or olfactory bulb of old mice (Figures S2K–S2M) (and there was also no impact on mouse behavior; see Figure 7C). This could be because RIPR-PD1 had opposing pro-aging and pro-inflammatory effects on other cell types in the SVZ niche, including endothelial cells, oligodendrocytes, and astrocytes/quiescent NSCs (qNSCs) (Figures 2S, S3J, S3K, and S3V), in agreement with previous reports on systemic anti-PD1.[13,40] Using immunostaining, we confirmed that RIPR-PD1 infusion increased the inflammation protein STAT1 in astrocytes/NSCs ($SOX2^+$ or $GFAP^+$) in the old SVZ (Figures 2T and S2N).

Thus, checkpoint inhibition in the brain locally increased the number of T cells and resulted in inflammation across many cell types of the old neurogenic niche, outweighing any potential benefits of T cell activation. Mitigating these pro-inflammatory effects of T cells may help restore old brain function.

An engineered IL-10 cytokine enhances anti-inflammatory pathways in old microglia

We used our platform to test whether restoring the balance in inflammatory pathways in microglia with the anti-inflammatory cytokine IL-10 could benefit the aged brain. Microglia express the IL-10 receptor, and IL-10 is very low in the brain[76] (Figure S4A), making IL-10 an intriguing candidate for exogenous administration. While IL-10 has anti-inflammatory effects on myeloid cells (e.g., microglia and macrophages), it can also act on T cells to induce IFN-γ and granzyme B[61,77–80] (Figure 3A). To uncouple the anti- and pro-inflammatory effects of IL-10, we used an engineered IL-10 variant (D25K, hereafter IL-10*), with decreased affinity for its receptor[60] (Figure 3A). In the periphery, this engineered IL-10* conserves anti-inflammatory effects on myeloid cells but has minimal effects on T cells.[60] However, the effects of this IL-10 variant on the brain have never been tested.

We continuously infused wild-type (WT) or engineered IL-10 (IL-10*) at two different concentrations (0.02 or 0.1 mg/mL) and vehicle alone (artificial cerebrospinal fluid) directly into the lateral ventricle of old mice (25 months, n = 1–2 male mice per condition, pooled). As a baseline control, we infused vehicle alone into the brain of young mice (3 months, n = 2 male mice, pooled). After 1 week, we performed scRNA-seq on the SVZ neurogenic niche (Figure 3B; Table S1). Importantly, we replicated our findings in an independent experiment with WT IL-10 (Figures S4L–S4Q; Table S1). There were no major differences in cell number or cell types in the SVZ (Figures 3C, S4B, and S4M; Table S1), although there was a strong transcriptional shift in old microglia in response to WT IL-10 and IL-10* (to a lesser extent) (Figures 3D and S4M).

Both WT IL-10 and IL-10* (to a lesser degree) elicited IL-10 signatures in microglia, including upregulation of *Stat3* and *Socs3* (Figures 3E, S4C, S4H, and S4N) and downregulation of class II antigen-presenting genes (*H2-DMa*, *H2-Oa*, and *H2-Ob*) and *Cd86*, known to be suppressed by IL-10[59–61] (Figure 3G). Importantly, both WT IL-10 and IL-10* strongly downregulated the pro-inflammatory cytokine genes *Tnf*, *Il1a*, and *Il6* (Figures 3F, 3G, S4C, S4H, and S4N). We experimentally validated that WT IL-10 and engineered IL-10* suppressed the secretion of IL-6 and

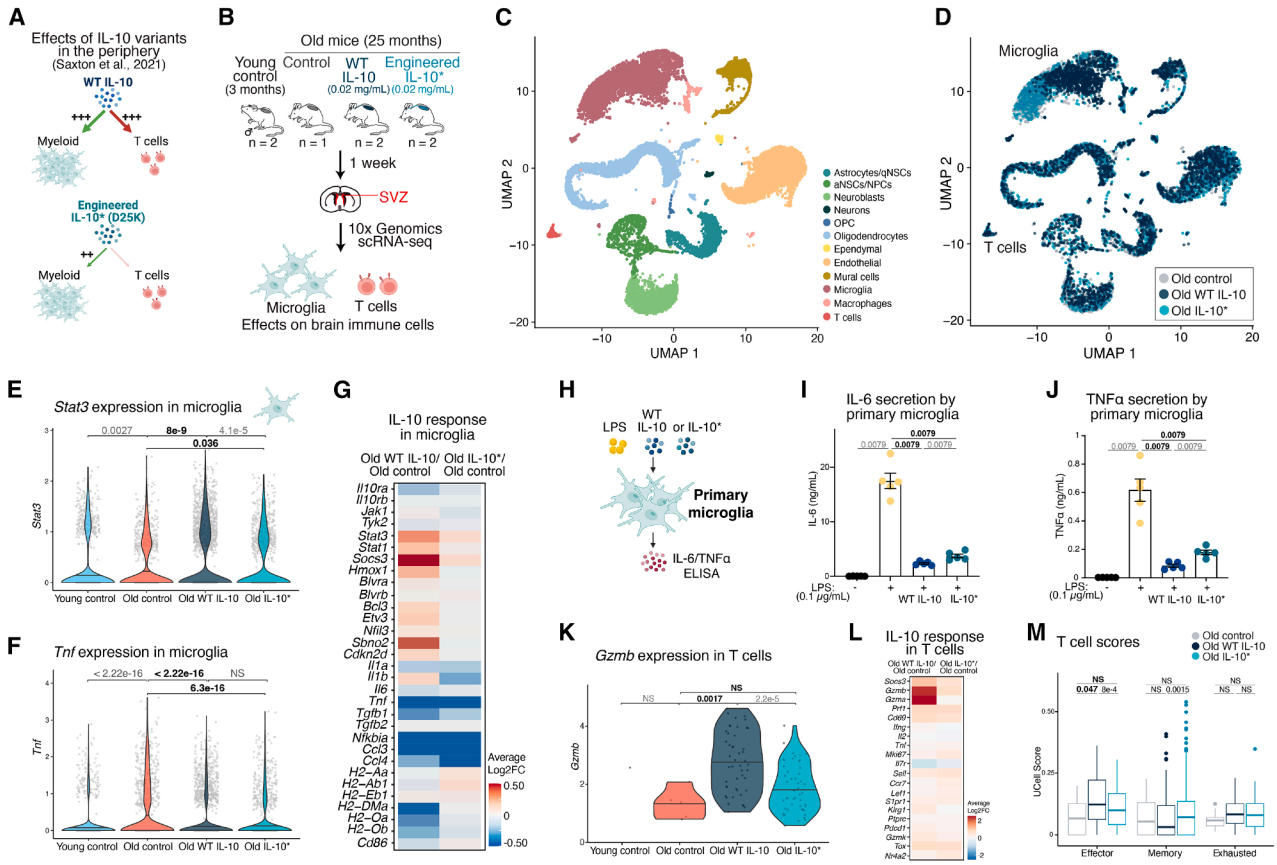

Figure 3. Enhancing anti-inflammatory pathways in microglia with engineered IL-10* cytokines

(A) Schematic depicting the pro- and anti-inflammatory effects of WT IL-10 and engineered IL-10* variant (D25K, IL-10*) on myeloid cells and T cells.

(B) Old male mice (25 months) were infused with vehicle control ($n = 1$), WT IL-10 (0.1 and 0.02 mg/mL, $n = 2$, pooled) or engineered IL-10* (0.1 and 0.02 mg/mL, $n = 2$, pooled). Young male mice (3 months, $n = 2$, pooled) were infused with vehicle control. scRNA-seq was performed as in Figure 2. Results with the higher concentration of IL-10 (0.1 mg/mL) are in Figures S4H–S4K. Figures 3, 4, S4B, S4C, and S4E are with the 0.02 mg/mL concentration.

(C) UMAP clustering of all high-quality cells downsampled to 3,365 cells per condition, colored by cell type.

(D) Same as (C), colored by condition.

(E and F) Log-normalized expression of IL-10 signaling genes *Stat3* (E) and *Tnf* (F) in microglia of the SVZ. Horizontal lines, median.

(G) Heatmap showing fold change in expression of genes in the IL-10 pathway in microglia. Red, upregulated; blue, downregulated genes with IL-10.

(H–J) Primary microglial cells were stimulated with lipopolysaccharide (LPS, 0.1 μg/mL) with or without WT IL-10 or IL-10* (10 mM) for 48 h. Amounts of secreted IL-6 (I) and TNF-α (J) cytokines were measured by ELISA. Data are mean ± SEM (see Table S4 for independent repeat).

(K) Log-normalized expression of *Gzmb* in T cells of the SVZ. Horizontal lines, median. Only T cells that expressed *Gzmb* were plotted.

(L) Heatmap as in (G) but for T cells.

(M) Each T cell was given a single score for each signature. Boxplot displays the median and lower and upper quartile values. Permutation-based *p* values; see STAR Methods.

p values, two-sided Wilcoxon rank-sum test, unless otherwise specified. NS, not significant.

See also Figure S4.

tumor necrosis factor alpha (TNF-α) in primary microglial cultures (and the microglial BV2 cell line) (Figures 3H–3J and S4D). Thus, both WT IL-10 and engineered IL-10* had strong anti-inflammatory effects on microglia.

IL-10 and engineered IL-10* have differential effects on T cells in old brains

T cells in the old SVZ also expressed the IL-10 receptor and thus could respond to IL-10 (see Figure S4A). Indeed, we observed a robust increase in the expression IL-10-induced genes (*Socs3*, *Gzmb*, and *Ifng*) and effector T cells genes (*Gzma*, *Cd69*, and *Prf1*) in T cells from old brains infused with WT IL-10 (Figures 3K, 3L, S4I, S4P, and S4Q). Importantly, this induction was attenuated with IL-10* (Figures 3K, 3L, and S4I). Consistently, effector T cell scores were increased in T cells from WT IL-10-treated but not from IL-10*-treated old mice (Figure 3M). Hence, the engineered IL-10* variant, unlike WT IL-10, did not strongly activate T cells in the old brain—providing a molecular handle to examine T cell contributions to brain aging.

Engineered IL-10* does not induce IFN signaling in old microglia

What is the net effect of IL-10 and the engineered IL-10* variant on microglial inflammatory pathways? WT IL-10 downregulated

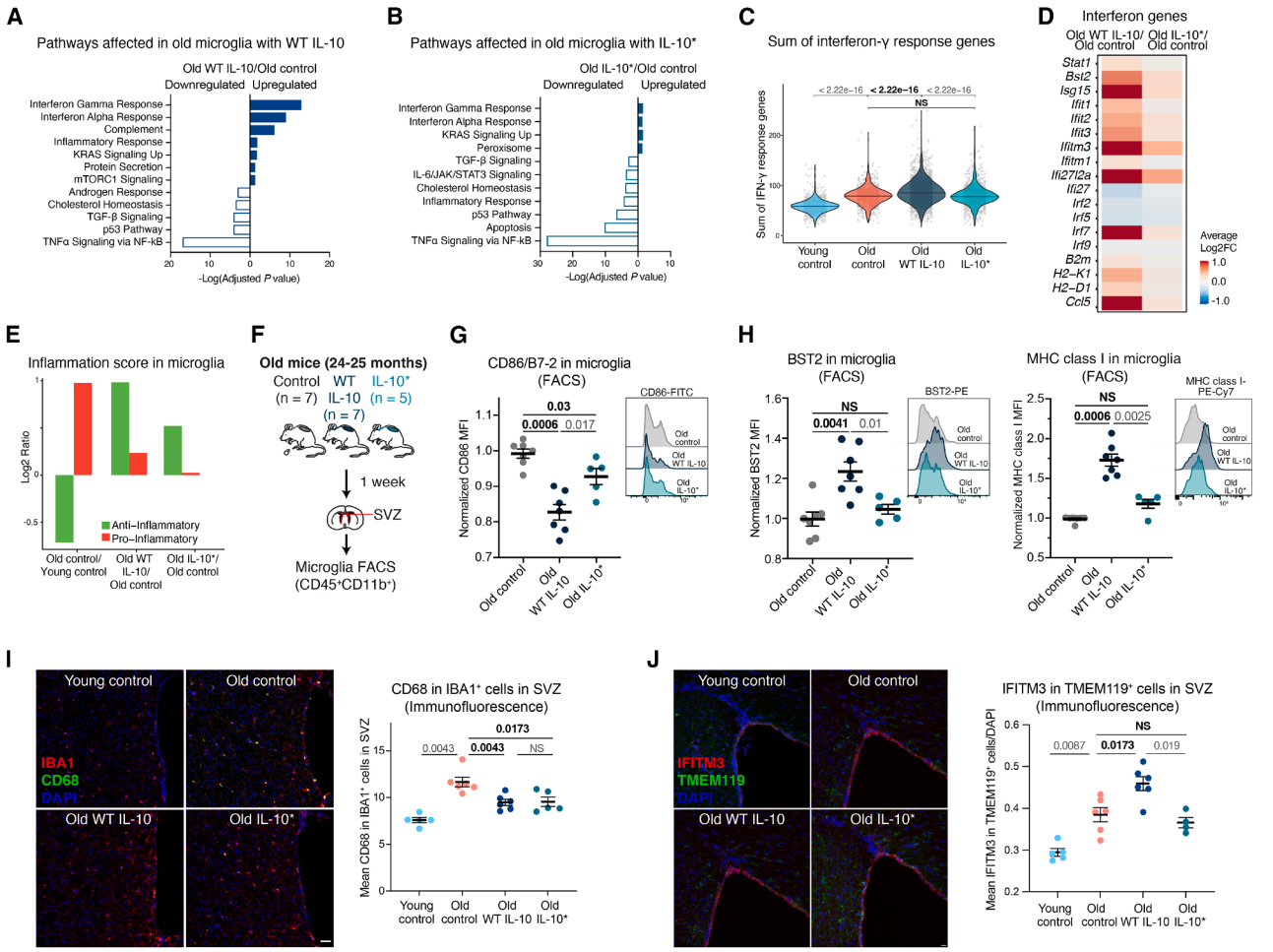

Figure 4. Net effect of engineered IL-10* cytokines on old microglia

(A and B) MSigDB hallmark pathways enriched in the top 100 differentially upregulated or downregulated genes in microglia from old mice treated with WT IL-10 (A) or IL-10* (B) vs. old control. For all pathways shown, FDR < 0.05, EnrichR statistics.

(C) Combined log-normalized expression of genes in the IFN-γ response pathway in microglia of the SVZ. Horizontal lines, median.

(D) Heatmap showing fold change in IFN response genes in microglia. Red, upregulated; blue, downregulated with IL-10.

(E) Inflammation scores for microglia in the SVZ of old control vs. young control, old WT IL-10 vs. old control, and old IL-10* vs. old control mice.

(F–H) Old male mice (24–25 months) were infused with vehicle control, WT IL-10, or engineered IL-10* for 1 week and FACS performed on microglia ($CD45^+$ $CD11b^+$). FACS quantification and representative histograms of CD86 (G), BST2 (H), and MHC class I (H) MFI in freshly isolated microglia (n = 5–7 mice combined over two independent experiments; see Table S4). MFI values (~3,000 microglial cells) were normalized to those of the median of old control for each experiment.

(I and J) Left, representative immunofluorescence images of CD68 and IBA1 (I) or IFITM3 and TMEM119 (J) in SVZ brain sections. Red, IFITM3 (IFN response) or IBA1 (microglia); green, CD68 (activation marker) or TMEM119 (microglia); blue, DAPI. Scale bar, 20 μm. Right, quantification of mean CD68 or IFITM3 fluorescence intensity overlapping with microglial cell marker fluorescence (IBA1 or TMEM119) in SVZ sections from young control (4 months, n = 5), old control (n = 6), old WT IL-10-treated (n = 6), and old IL-10*-treated (n = 4–5) male mice (24 months). Each dot represents one mouse (average of three coronal sections per mouse). One independent experiment.

Data are mean ± SEM. p values, two-sided Wilcoxon rank-sum test. NS, not significant.

See also Figure S4.

pro-inflammatory TNF-α signaling but also strongly upregulated IFN signaling (Figures 4A, 4C, 4D, S4J, and S4O; Table S2). By contrast, the engineered IL-10* suppressed TNF-α signaling genes without markedly upregulating IFN signaling in aged microglia (Figures 4B–4D and S4J; Table S2). We observed similar patterns when calculating "inflammation scores" (Figure 4E), confirming that IL-10* is more anti-inflammatory overall, even in the context of elevated T cell numbers in the old brain.

We validated the effects of WT IL-10 and IL-10* on microglia by measuring inflammation-related proteins. FACS analysis (Figure 4F) showed that WT IL-10 infusion into the brain reduced CD86/B7-2 in old microglia (Figure 4G) but strongly increased IFN markers BST2 and MHC class I (Figures 4H and S4F). The IL-10* variant still reduced CD86/B7-2, without inducing BST2 or MHC class I in old microglia (Figures 4G, 4H, and S4G). Similarly, immunostaining showed that WT IL-10 decreased the microglial activation marker CD68/macrosialin (Figure 4I), but it strongly increased IFN-induced proteins IFITM3 and STAT1 in microglia of the old SVZ (Figures 4J and S4G). In contrast, the IL-10* variant suppressed

CD68/macrosialin, without inducing STAT1 or IFITM3 in old SVZ microglia (Figures 4I, 4J, and S4G).

Thus, WT IL-10 suppressed microglial activation but also triggered pro-inflammatory IFN pathways in aged microglia, likely via T cells. By suppressing microglial activation without inducing IFN responses, the engineered IL-10* variant restored the inflammatory balance in aged microglia.

IL-10-induced IFN signaling in microglia is partly mediated by T cells

Could the pro-inflammatory IFN signaling induced in microglia by WT IL-10 be due to T cells and their secretion of IFN-γ, as T cells were the predominant cell type expressing *Ifng* (IFN-γ) within the old SVZ niche (see Figure S4E)? To test the effects of IL-10 on microglia in the context of T cells, we set up an *in vitro* co-culture system (Figure 5A). We first verified IL-10 signaling in mouse primary T cells, primary microglia, and the BV2 microglial cell line (Figures S5A–S5G). We then cultured mouse primary microglia (or BV2 cells) with or without T cells and WT IL-10 or engineered IL-10* for 72 h and measured IFN markers (BST2 and MHC class I) on microglia by FACS (Figure 5A). In the absence of T cells, WT IL-10 and engineered IL-10* did not increase BST2 on microglia (Figure 5B), and MHC class I was only slightly increased (Figure 5C). In the presence of T cells, WT IL-10 significantly increased BST2 and MHC class I in primary microglia (Figures 5B and 5C), whereas the engineered IL-10* variant did not (Figures 5B and 5C). This effect of WT IL-10 was blocked by the addition of an antibody that neutralizes IFN-γ (Figures 5E and 5F), indicating that it is mediated by IFN-γ. We observed similar results with the BV2 microglial cell line (Figures S5H–S5J) and by immunostaining (Figure 5D). Indeed, WT IL-10 increased the secretion of IFN-γ (and granzyme B) by T cells while IL-10* did not (Figures S5K and S5L; IFN-α and IFN-β were undetectable), consistent with our observations *in vivo* in the brain.

We also tested whether IL-10 could potentiate IFN-γ signaling in microglia. Primary microglia treated with IFN-γ and WT IL-10 showed increased IFN signaling, while IL-10* caused only a trending increase (Figures S5M and S5N). Thus, IL-10 likely amplifies IFN signaling in microglia by increasing IFN-γ secretion by T cells and potentiating the IFN-γ response (Figure S5P).

To test the importance of IFNs in the IL-10 response *in vivo*, we infused old brains with WT IL-10 together with a blocking IFN-γ antibody and measured IFN signaling in microglia by FACS (Figure S5O). We observed a trending (non-significant) decrease in BST2 and MHC class I in old microglia infused with WT IL-10 and anti-IFN-γ, compared with control anti-immunoglobulin G (IgG) antibodies (Figure S5O), suggesting that other IFNs could contribute to this effect. To block all IFN signaling, we combined antibodies against IFN-γ and the IFN-α/β receptor (IFNAR) together with WT IL-10. With both blocking antibodies, IFN signaling was no longer induced in old SVZ microglia in response to WT IL-10 (Figures 5G–5I). Thus, the concerted action of WT IL-10, IFN-γ (secreted by T cells), and IFN-α and IFN-β (possibly secreted by the choroid plexus[39]) may potentiate IFN signaling in microglia in the aged brain (Figure S5P). The engineered IL-10 variant, by limiting T cell activation and IFN signaling, helps break this negative inflammatory loop in aged brains.

Engineered IL-10* improves neurogenesis in old mice

We examined the effects of WT IL-10 and engineered IL-10* on other cell types of the neurogenic niche. Overall, 'aging clocks' predicted IL-10* to have a more pro-rejuvenating effect compared to WT IL-10 across several cell types (Figures 6A, S6A, S6B, and S4K). Consistently, IFN and immune pathways were more upregulated by WT IL-10 than IL-10* in oligodendrocytes and in astrocytes/qNSCs (Figures 6B and 6D; Table S3). Immunostaining confirmed that WT IL-10 strongly induced the IFN marker STAT1 in oligodendrocytes ($OLIG2^+$) whereas IL-10* did not (Figure 6E).

Aging clocks predicted mild "rejuvenation" of aNSCs/NPCs and neuroblasts with both WT IL-10 and engineered IL-10* (Figures 6A, S6A, S6B, and S4K). In line with this, cell proliferation and cell junction pathways were upregulated in aNSCs/NPCs (Figure 6C; Table S3). We assessed the function of NSCs in the old SVZ by quantifying neurogenesis[75,81] (Figure 6F). WT IL-10 and engineered IL-10* both increased neuroblasts (DCX^+) in the old SVZ (Figure 6G) and neural progenitors (DCX^+EdU^+) in the olfactory bulb (Figures 6H and 6I). Notably, the IL-10* variant also induced a small increase in the number of newborn neurons (EdU^+NeuN^+) in the olfactory bulb of old mice (Figures 6H and 6J). Therefore, WT IL-10 and engineered IL-10* enhance NSC function in the aged SVZ, with IL-10* further promoting neurogenesis—likely through a combination of effects across multiple niche cell types. To integrate the effects of WT IL-10 and IL-10* on the SVZ neurogenic niche as a whole, we measured changes in principal-component analysis (PCA) space (Figure S6C). While WT IL-10 had little effect, IL-10* shifted the niche toward a more "youthful" profile (Figures 6K, S6D, and S6E), consistent with its beneficial effect on neurogenesis.

Thus, the engineered IL-10* variant is more "pro-rejuvenating" in the old SVZ neurogenic niche, likely by restoring the overall balance in inflammation in the aged niche.

Engineered IL-10* rescues behaviors impaired with age in mice

Could immune-based interventions improve functional outcomes in behaviors that decline with age in mice? We first used nest-building behavior, which is impaired in mice during aging,[82,83] as an indicator of well-being and to anticipate potential cognitive improvements in aged mice. We delivered immune interventions into the brain and gave mice 48 h to build nests (Figure 7A). As expected, old mice showed a significant decline in nest-building behavior, compared with young mice (Figure 7B). Notably, engineered IL-10* significantly improved nesting behavior, compared with control (Figure 7B), while WT IL-10 (and RIPR-PD1) did not (Figures 7B and 7C).

Based on these results, we assessed whether IL-10* could improve cognitive function in aged mice, as other immune-based interventions have done.[84–88] We infused control vehicle or engineered IL-10* into the brain of old male mice for a week (21 months, n = 15 mice per group), allowed an additional week for recovery, and then performed the forced alternation Y maze test followed by the novel object recognition (NOR) test, after which brains were collected for staining (Figure 7D). No differences in overall activity were detected between control and IL-10*-treated groups in the open field test (Figure 7E), indicating

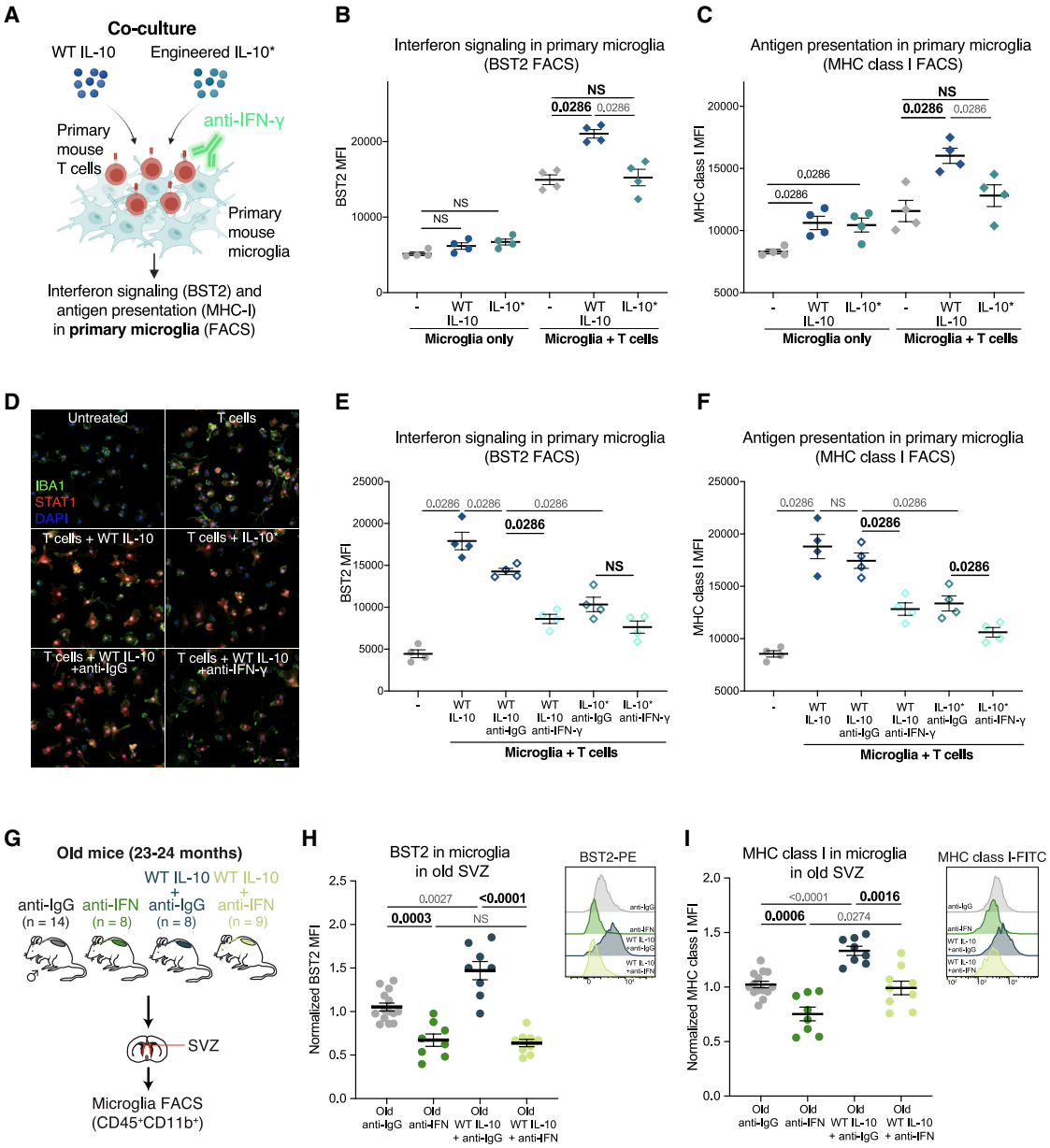

Figure 5. IL-10-induced IFN pathway response in microglia is likely due to T cell activation

(A) Scheme for the co-culture of mouse primary microglia with mouse primary T cells and WT IL-10 or IL-10* (10 nM) for 72 h. IFN signaling was measured by FACS.

(B and C) FACS quantification of BST2 (B) and MHC class I (C) MFI in ~10,000–20,000 mouse primary microglia from 4 individual cultures (see Table S4 for independent repeat).

(D) Representative immunofluorescence images of primary microglia co-cultures. Green, IBA1 (microglia); red, STAT1 (IFN response); blue, DAPI. Scale bar, 20 μm.

(E and F) FACS quantification as in (B and C).

(G–I) Old male mice (23–24 months) were infused with anti-IgG control or anti-IFN antibodies (1mg/mL) and WT IL-10 (0.02 mg/mL) for 1 week. FACS quantification and histograms of BST2 (H) and MHC class I (I) MFI in microglia ($CD45^+CD11b^+$) freshly isolated from the SVZ (n = 8–14 combined over three independent experiments; see Table S4). Each dot represents one mouse (MFI from ~1,500 microglial cells per mouse). MFI values were normalized to old control anti-IgG for each experiment.

Data are mean ± SEM. p values, two-sided Wilcoxon rank-sum test. NS, not significant.

See also Figure S5.

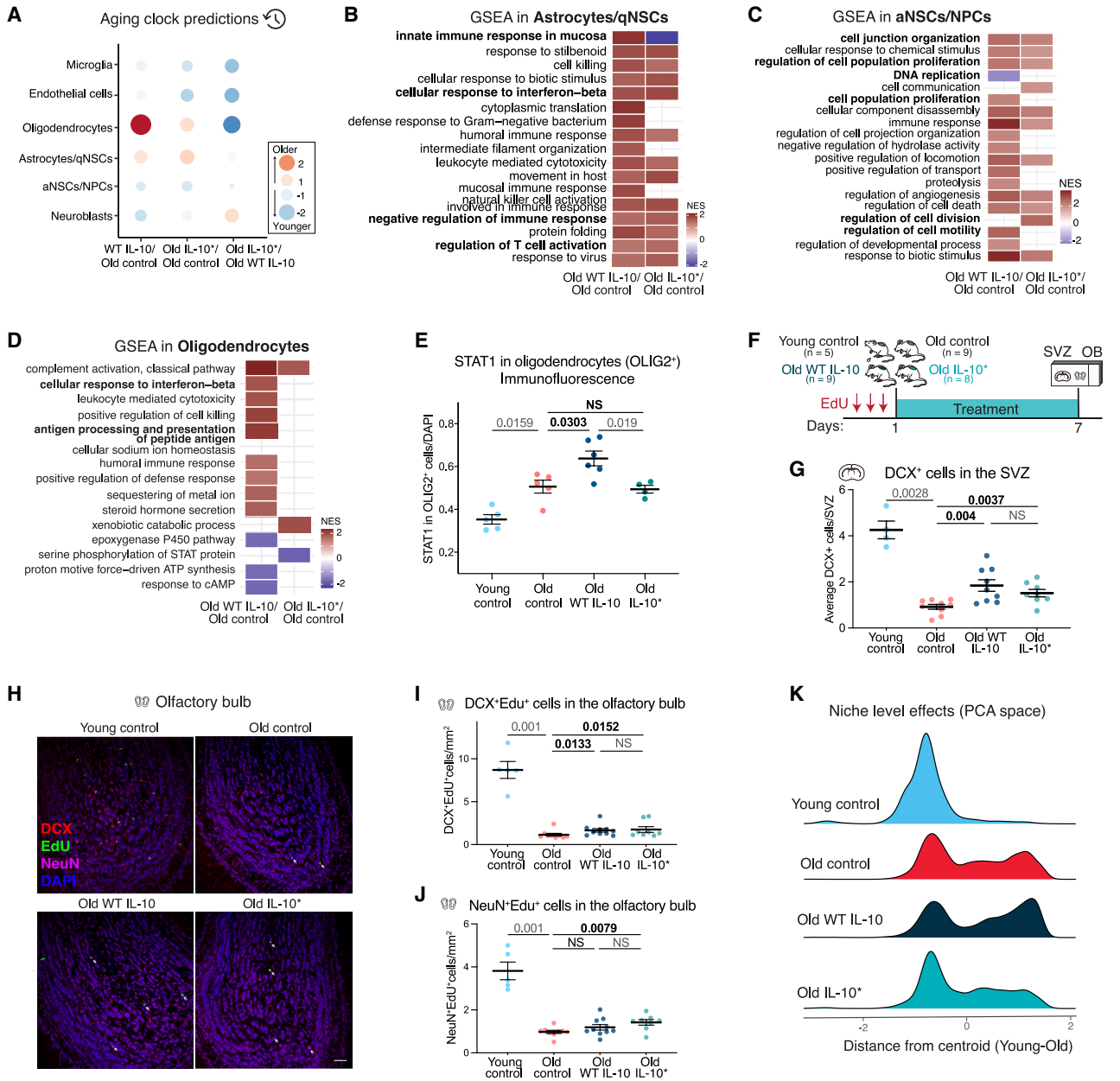

Figure 6. Impact of engineered IL-10* cytokines on the old neurogenic niche

(A) Effects of WT IL-10 and IL-10* on aging clock[51] predictions for SVZ cells.

(B) Heatmaps of gene set enrichment analysis in WT IL-10 and IL-10* vs. old control astrocytes/qNSCs. Normalized enrichment scores for each pathway with FDR < 0.05. Red, enriched in IL-10 vs. control; blue, enriched in control vs. IL-10.

(C) Same as (B), for aNSCs/NPCs.

(D) Same as (B), for oligodendrocytes.

(E) Quantification of STAT1 fluorescence overlapping with oligodendrocyte marker (OLIG2) in SVZ brain sections of young control (4 months, $n = 5$), old control ($n = 5$), old WT IL-10 ($n = 6$), and old IL-10* ($n = 4$) male mice (24 months). Each dot represents one mouse (average of three coronal sections per mouse). One independent experiment.

(F) Neurogenesis assay. Mice were injected intraperitoneally with EdU for 3 days, and mini-osmotic pumps were implanted. After 1 week, brains were processed for immunostaining.

(G) Quantification of DCX$^+$ cells in SVZ brain sections from young control (4 months, $n = 4$) and old control, WT IL-10-treated, or IL-10*-treated male mice (24–27 months, $n = 8$–9, combined over two independent experiments; see Table S4). Each dot represents one mouse (average of three coronal sections per mouse).

(H) Representative immunofluorescence images of the olfactory bulb. Red, DCX (neural progenitors); green, EdU (proliferating cells); magenta, NeuN (neurons); blue, DAPI. Scale bar, 50 μm.

(I and J) Number of neural progenitors (DCX$^+$EdU$^+$) (I) and newborn neurons (NeuN$^+$EdU$^+$) (J) per mm^2 in the olfactory bulb (same mice as G). Each dot represents one mouse (average of six coronal sections per mouse).

(legend continued on next page)

that anxiety was not affected. In the forced alternation Y maze, which measures short-term spatial working memory, old control mice showed no preference for the novel arm (Figures 7F and 7G), while old mice infused with IL-10* explored the novel arm more often (Figures 7F and 7G; Table S4). In the NOR test, old control mice showed no preference for exploring the novel or familiar object, while old mice infused with IL-10* spent significantly more time exploring the novel object (Figure 7H; Table S4). Thus, IL-10* causes some improvements in memory in old mice.

We tested whether microglial inflammatory state was changed in brain regions linked to these cognitive tests,[89,90] such as the hippocampus. Immunostaining of the hippocampus showed that IL-10* decreased CD68/macrosialin in microglia (Figures 7I and 7J) without inducing IFN signaling (Figure S6F). This indicates that IL-10* uncouples anti-inflammatory and pro-inflammatory signaling in hippocampal microglia (although the effects of IL-10* on neurons remain to be tested).

Overall, direct delivery of engineered IL-10* into the old brain reduces microglial activation across different brain regions and attenuates age-related behavioral impairments in mice, suggesting engineered IL-10* as a potential immunotherapy for the aged brain.

DISCUSSION

Here, we build a platform to test targeted immune-based interventions directly in the old brain. Manipulating immune cells and inflammatory pathways has been previously found to impact the old brain,[12,13,28,30,37–39] but these attempts relied on broad interventions, often performed in the periphery. We find that delivery of a potent engineered checkpoint inhibitor (RIPR-PD1) directly into the brain increases the number of T cells and promotes microglial inflammation. While T cells are not numerous in the brain, their migratory nature and influence on other cells could amplify immune responses beyond the initial cells. Checkpoint inhibitor infusion in the brain triggers inflammation and pro-aging signatures across many cell types in the old neurogenic niche, consistent with the observation that T cells have a spatial pro-aging proximity effect on their neighbors.[7] Activated NSCs/NPCs and neuroblasts are mostly spared from the negative impact of T cell activation, perhaps because activated T cells also remove dysfunctional NSCs, as observed in other contexts.[41,44,91] In the old brain, T cell exhaustion might in fact represent a mechanism to prevent aberrant inflammation, as proposed in the skin.[92] As diverse T cell populations populate the brain,[93–102] targeting specific T cell pools could help counter brain aging.

To restore the balance in inflammatory pathways in aged microglia, we use the anti-inflammatory cytokine IL-10. IL-10 generates potent anti-inflammatory responses in microglia, but it also induces pro-inflammatory pathways. This pro-inflammatory response is partly mediated by T cells, together with synergizing effects between IL-10 and interferons in microglia. Our results may explain the conflicting results observed with IL-10 in Alzheimer's disease,[103–108] given the elevated T cell infiltration in Alzheimer's disease brains.[18–20,22,23] Notably, an engineered IL-10* variant (D25K), which still generates anti-inflammatory responses in microglia but does not activate T cells, has a rejuvenating effect on the old SVZ neurogenic niche, improving NSC function and neurogenesis. Old mice treated with this engineered IL-10* variant also showed improved nest-building behavior and cognitive function, but whether this is mediated by direct or indirect effects on neurons remains to be tested.

Overall, our study provides evidence that immune-based interventions promoting anti-inflammatory pathways in microglia while suppressing T cells could help counter brain aging and age-related diseases. Immunotherapies have revolutionized cancer treatment[64,66,67] and are emerging for aging.[109–112] Excitingly, age-related immune changes observed in mice also occur in humans,[52,53] supporting the idea that anti-aging immunotherapies could be translated to humans.

Limitations of the study

All experiments were conducted in male mice. Conducting these experiments in female mice could help to identify sex-specific differences and to generalize our findings. Moreover, surgical implantation of mini-osmotic pumps for brain delivery is invasive and could cause immune cell infiltration and inflammation. Developing engineered proteins that can cross the blood-brain barrier could eliminate the need for surgery in the future. Finally, we did not identify the specific cells or factors that mediate the beneficial effects of the engineered IL-10* variant on cognition. Targeting specific cell types and their secreted factors could help determine the mechanism of IL-10 action on cognitive function.

RESOURCE AVAILABILITY

Lead contact

Requests for further information and resources should be directed to and will be fulfilled by the lead contact, Anne Brunet (abrunet1@stanford.edu).

Materials availability

This study did not generate new unique reagents.

Data and code availability

- All raw sequencing reads for scRNA-seq data can be found under BioProject PRJNA1365936. Processed Seurat objects are available on Zenodo: https://doi.org/10.5281/zenodo.17594828. Data are publicly available from the date of publication.
- Code is publicly available on GitHub: https://github.com/PalomaNavarro/TargetingImmuneCellsSVZ and Zenodo: https://doi.org/10.5281/zenodo.18174039.
- Any additional information required to reanalyze data reported in this paper will be available from the lead contact.

(K) Effects of age and interventions in PCA space. Ridge plots represent the cell density distribution. *x* axis indicates Mahalanobis distance of a given cell relative to the centroid of young and old control niche cells.
Data are mean ± SEM. *p* values, two-sided Wilcoxon rank-sum test. NS, not significant.
See also Figure S6.

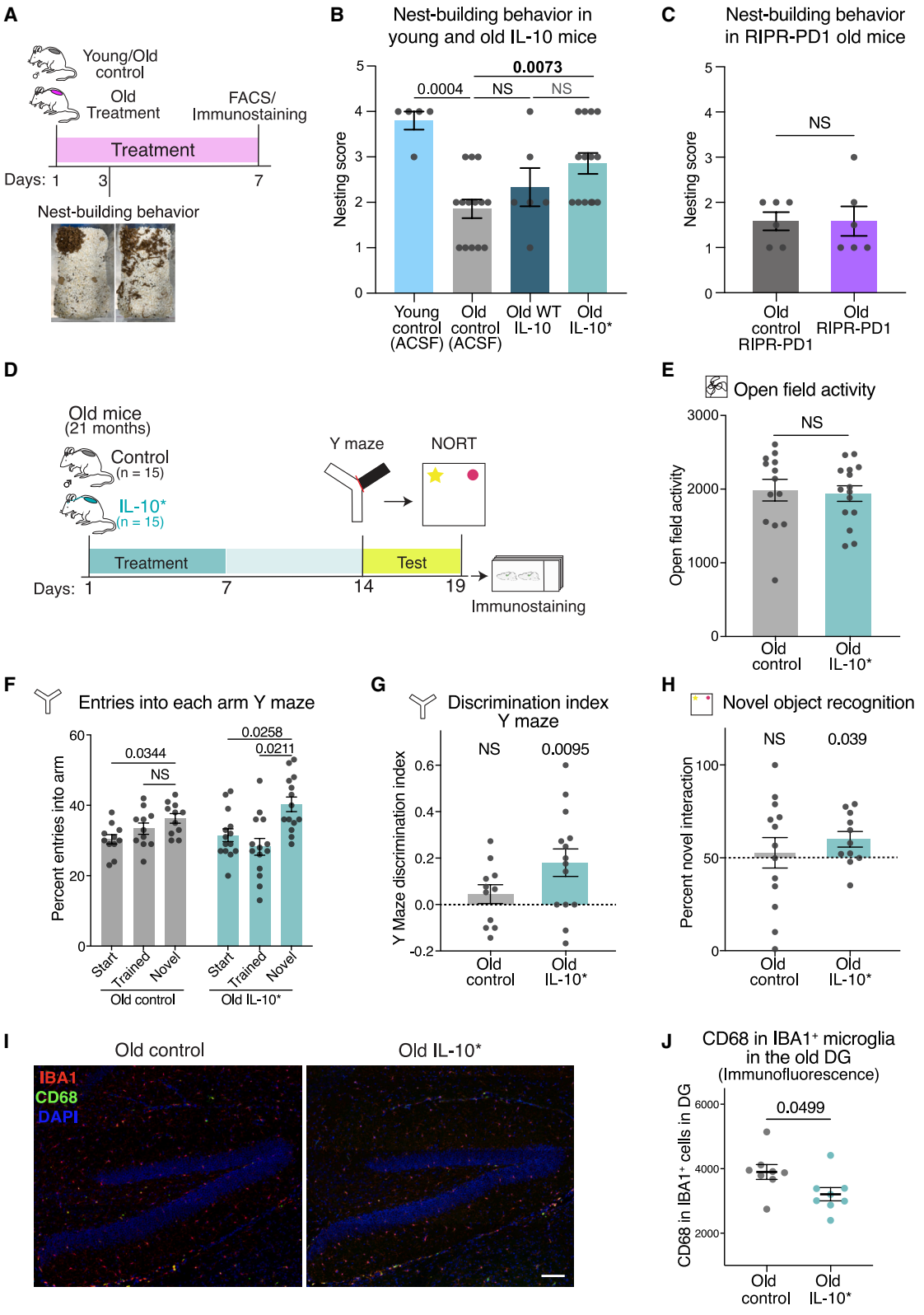

Figure 7. Impact of immune-based interventions on mouse behavior and cognition

(A) Mice were provided with unstructured nestlet material and given 48 h to build nests after surgery. Nesting scores, 1 = no nest (right picture); 4 = enclosed nest (left picture).

(legend continued on next page)

ACKNOWLEDGMENTS

We thank all members of the Brunet lab for helpful discussions, particularly B. Ameglio, J.W. Miklas, R. Nagvekar, and J. Yang. FACS was performed at the Stanford FACS Facility supported by NIH S10RR025518-01, S10RR027431-01, and S10OD026831-01. Some illustrations were created with BioRender.com. The authors gratefully acknowledge support as follows: NIH R01AG071711 (A.B.); a generous gift from T. and M. Barakett (A.B.); CZI inflammation grant (A.B. and K.C.G.); Knight Initiative for Brain Resilience Innovation award (A.B. and K.C.G.); Simons Foundation and NIA grants AG077816 (S.A.V.), AG064823 (A.B.S.), and AG086042 (J.S.); Wellcome Trust Sir Henry Wellcome Fellowship WT101609MA (R.A.F.); Chinese Academy of Medical Sciences Innovation Fund for Medical Science Grant 2018-I2M-2-002 (R.A.F); and Human Frontiers Science Program Long-Term Fellowship (P.N.N).

AUTHOR CONTRIBUTIONS

P.N.N. and A.B. planned the study, with intellectual contributions from R.A.S., R.A.F., and K.C.G. P.N.N. designed, performed, and analyzed most experiments. J.Y. helped with immunofluorescence, ELISAs, and nesting assays. M.H. performed BV2 co-culture experiments and ELISAs. A.B.S. performed Y maze and NOR experiments with help from J.S.C. and under the guidance of S.A.V. D.J.R. performed some scRNA-seq analysis. R.A.S. and G.C.A. produced IL-10 proteins under K.C.G. supervision. A.P.T. generated primary microglia cultures with help from E.R.L. and under the supervision of T.W.-C. E.D.S. performed MERFISH analysis. G.N. helped with T cell FACS analysis. J.R.-M. helped with neurogenesis experiments. O.Y.Z. and L.X. helped with collections for FACS and 10× experiments. M.T.B. helped with scRNA-seq of brain T cells. K.E.M. helped with immunofluorescence. L.P. and R.A.F. produced RIPR-PD1 proteins, under the supervision of K.C.G. J.Y., M.H., and J.R.-M. assisted with surgeries. E.D.S., O.Y.Z, and L.X. independently checked code. P.N.N. and A.B. wrote the manuscript, and all authors provided comments.

DECLARATION OF INTERESTS

K.C.G. and R.A.F. are inventors on a patent involving RIPR-PD1 (WO2019222547A1). K.C.G. and R.A.S. are inventors on a patent involving IL-10 (WO2021243057A1). K.C.G. is the founder of Synthekine Inc. A.B. is on the Scientific Advisory Board of Calico Labs.

STAR★METHODS

Detailed methods are provided in the online version of this paper and include the following:

SUPPLEMENTAL INFORMATION

Supplemental information can be found online at https://doi.org/10.1016/j.immuni.2026.01.016.

Received: July 22, 2024
Revised: September 19, 2025
Accepted: January 9, 2026
Published: January 30, 2026

REFERENCES

1. Gaspar-Silva, F., Trigo, D., and Magalhaes, J. (2023). Ageing in the brain: mechanisms and rejuvenating strategies. Cell. Mol. Life Sci. *80*, 190. https://doi.org/10.1007/s00018-023-04832-6.

(B) Nesting scores for young control (4 months, $n = 5$) and old control, old WT IL-10-treated, and old IL-10*-treated male mice (22–24 months, $n = 6$–14; see Table S4 for independent experiments).
(C) Nesting scores for old control and RIPR-PD1-treated (25 months, $n = 6$) male mice. One independent experiment.
(D) Vehicle control or IL-10* was delivered into the lateral ventricle of old male mice (21 months) with mini-osmotic pumps for a week. A week later, behavioral testing was performed and brains were processed for immunostaining. Two mice from the control group died before testing. One independent experiment.
(E) Baseline activity assessed with open field test in old control ($n = 13$) and old IL-10*-treated ($n = 15$) male mice (21 months).
(F) Percentage of entries into each of the arms of the Y maze for old control ($n = 11$) and old IL-10*-treated ($n = 14$) male mice (21 months). Two control and one IL-10* mice did not perform three entries during the first minute and were excluded. p values, two-way ANOVA with Sidák's post hoc test.
(G) Discrimination index for the novel vs. the familiar arm (as in F). p values, two-tailed one-sample t tests.
(H) Percentage of time exploring the novel object in old control ($n = 13$) and old IL-10*-treated ($n = 11$) male mice (21 months). p values, two-tailed one-sample t tests.
(I and J) Representative immunofluorescence images (I) and quantification (J) of CD68 fluorescence overlapping with IBA1 in sagittal brain sections of the hippocampus from old control and old IL-10*-treated (21 months, $n = 8$) male mice after behavioral testing. Red, IBA1 (microglia); green, CD68 (activation marker); blue, DAPI. Scale bar, 50 μm. Each dot represents one mouse (average of two sagittal sections per mouse).
For all panels, each dot is one mouse. Data are mean ± SEM. p values, two-sided Wilcoxon rank-sum test, unless otherwise specified. NS, not significant.
See also Figure S6.

2. Mattson, M.P., and Arumugam, T.V. (2018). Hallmarks of Brain Aging: Adaptive and Pathological Modification by Metabolic States. Cell Metab. *27*, 1176–1199. https://doi.org/10.1016/j.cmet.2018.05.011.

3. McAvoy, K.M., and Sahay, A. (2017). Targeting Adult Neurogenesis to Optimize Hippocampal Circuits in Aging. Neurotherapeutics *14*, 630–645. https://doi.org/10.1007/s13311-017-0539-6.

4. Sun, E.D., Nagvekar, R., Pogson, A.N., and Brunet, A. (2025). Brain aging and rejuvenation at single-cell resolution. Neuron *113*, 82–108. https://doi.org/10.1016/j.neuron.2024.12.007.

5. Ritzel, R.M., Crapser, J., Patel, A.R., Verma, R., Grenier, J.M., Chauhan, A., Jellison, E.R., and McCullough, L.D. (2016). Age-Associated Resident Memory CD8 T Cells in the Central Nervous System Are Primed To Potentiate Inflammation after Ischemic Brain Injury. J. Immunol. *196*, 3318–3330. https://doi.org/10.4049/jimmunol.1502021.

6. Stichel, C.C., and Luebbert, H. (2007). Inflammatory processes in the aging mouse brain: participation of dendritic cells and T-cells. Neurobiol. Aging *28*, 1507–1521. https://doi.org/10.1016/j.neurobiolaging.2006.07.022.

7. Sun, E.D., Zhou, O.Y., Hauptschein, M., Rappoport, N., Xu, L., Navarro Negredo, P., Liu, L., Rando, T.A., Zou, J., and Brunet, A. (2025). Spatial transcriptomic clocks reveal cell proximity effects in brain ageing. Nature *638*, 160–171. https://doi.org/10.1038/s41586-024-08334-8.

8. Dulken, B.W., Buckley, M.T., Navarro Negredo, P., Saligrama, N., Cayrol, R., Leeman, D.S., George, B.M., Boutet, S.C., Hebestreit, K., Pluvinage, J.V., et al. (2019). Single-cell analysis reveals T cell infiltration in old neurogenic niches. Nature *571*, 205–210. https://doi.org/10.1038/s41586-019-1362-5.

9. Zhang, X., Wang, R., Chen, H., Jin, C., Jin, Z., Lu, J., Xu, L., Lu, Y., Zhang, J., and Shi, L. (2022). Aged microglia promote peripheral T cell infiltration by reprogramming the microenvironment of neurogenic niches. Immun. Ageing *19*, 34. https://doi.org/10.1186/s12979-022-00289-6.

10. Ziv, Y., Ron, N., Butovsky, O., Landa, G., Sudai, E., Greenberg, N., Cohen, H., Kipnis, J., and Schwartz, M. (2006). Immune cells contribute to the maintenance of neurogenesis and spatial learning abilities in adulthood. Nat. Neurosci. *9*, 268–275. https://doi.org/10.1038/nn1629.

11. Moreno-Valladares, M., Moreno-Cugnon, L., Silva, T.M., Garcés, J.P., Saenz-Antoñanzas, A., Álvarez-Satta, M., and Matheu, A. (2020). CD8(+) T cells are increased in the subventricular zone with physiological and pathological aging. Aging Cell *19*, e13198. https://doi.org/10.1111/acel.13198.

12. Groh, J., Knöpper, K., Arampatzi, P., Yuan, X., Lößlein, L., Saliba, A.E., Kastenmüller, W., and Martini, R. (2021). Accumulation of cytotoxic T cells in the aged CNS leads to axon degeneration and contributes to cognitive and motor decline. Nat Aging *1*, 357–367. https://doi.org/10.1038/s43587-021-00049-z.

13. Kaya, T., Mattugini, N., Liu, L., Ji, H., Cantuti-Castelvetri, L., Wu, J., Schifferer, M., Groh, J., Martini, R., Besson-Girard, S., et al. (2022). CD8+ T cells induce interferon-responsive oligodendrocytes and microglia in white matter aging. Nat. Neurosci. *25*, 1446–1457. https://doi.org/10.1038/s41593-022-01183-6.

14. Moreno-Valladares, M., Silva, T.M., Garcés, J.P., Saenz-Antoñanzas, A., Moreno-Cugnon, L., Álvarez-Satta, M., and Matheu, A. (2020). CD8(+) T cells are present at low levels in the white matter with physiological and pathological aging. Aging (Albany, NY) *12*, 18928–18941. https://doi.org/10.18632/aging.104043.

15. Smolders, J., Heutinck, K.M., Fransen, N.L., Remmerswaal, E.B.M., Hombrink, P., ten Berge, I.J.M., van Lier, R.A.W., Huitinga, I., and Hamann, J. (2018). Tissue-resident memory T cells populate the human brain. Nat. Commun. *9*, 4593. https://doi.org/10.1038/s41467-018-07053-9.

16. Groh, J., Feng, R., Yuan, X., Liu, L., Klein, D., Hutahaean, G., Butz, E., Wang, Z., Steinbrecher, L., Neher, J., et al. (2025). Microglia activation orchestrates CXCL10-mediated CD8+ T cell recruitment to promote aging-related white matter degeneration. Nat. Neurosci. *28*, 1160–1173. https://doi.org/10.1038/s41593-025-01955-w.

17. Pappalardo, J.L., Zhang, L., Pecsok, M.K., Perlman, K., Zografou, C., Raddassi, K., Abulaban, A., Krishnaswamy, S., Antel, J., van Dijk, D., et al. (2020). Transcriptomic and clonal characterization of T cells in the human central nervous system. Sci. Immunol. *5*, eabb8786. https://doi.org/10.1126/sciimmunol.abb8786.

18. Chen, X., Firulyova, M., Manis, M., Herz, J., Smirnov, I., Aladyeva, E., Wang, C., Bao, X., Finn, M.B., Hu, H., et al. (2023). Microglia-mediated T cell infiltration drives neurodegeneration in tauopathy. Nature *615*, 668–677. https://doi.org/10.1038/s41586-023-05788-0.

19. Fernando, N., Gopalakrishnan, J., Behensky, A., Reich, L., Liu, C., Bass, V., Bono, M., Montgomery, W., De Pace, R., Mattapallil, M., et al. (2023). Single-cell multiomic analysis reveals the involvement of Type I interferon-responsive CD8+ T cells in amyloid beta-associated memory loss. Preprint at bioRxiv. 2023.03.18.533293. https://doi.org/10.1101/2023.03.18.533293.

20. Gate, D., Saligrama, N., Leventhal, O., Yang, A.C., Unger, M.S., Middeldorp, J., Chen, K., Lehallier, B., Channappa, D., De Los Santos, M.B., et al. (2020). Clonally expanded CD8 T cells patrol the cerebrospinal fluid in Alzheimer's disease. Nature *577*, 399–404. https://doi.org/10.1038/s41586-019-1895-7.

21. Piehl, N., van Olst, L., Ramakrishnan, A., Teregulova, V., Simonton, B., Zhang, Z., Tapp, E., Channappa, D., Oh, H., Losada, P.M., et al. (2022). Cerebrospinal fluid immune dysregulation during healthy brain aging and cognitive impairment. Cell *185*, 5028–5039.e13. https://doi.org/10.1016/j.cell.2022.11.019.

22. Su, W., Saravia, J., Risch, I., Rankin, S., Guy, C., Chapman, N.M., Shi, H., Sun, Y., Kc, A., Li, W., et al. (2023). CXCR6 orchestrates brain CD8(+) T cell residency and limits mouse Alzheimer's disease pathology. Nat. Immunol. *24*, 1735–1747. https://doi.org/10.1038/s41590-023-01604-z.

23. Altendorfer, B., Unger, M.S., Poupardin, R., Hoog, A., Asslaber, D., Gratz, I.K., Mrowetz, H., Benedetti, A., de Sousa, D.M.B., Greil, R., et al. (2022). Transcriptomic Profiling Identifies CD8(+) T Cells in the Brain of Aged and Alzheimer's Disease Transgenic Mice as Tissue-Resident Memory T Cells. J. Immunol. *209*, 1272–1285. https://doi.org/10.4049/jimmunol.2100737.

24. Mason, H.D., Latour, Y.L., Boughter, C.T., Johnson, K.R., Maric, D., Dorrier, C.E., Guedes, V.A., Lai, C., Duncker, P.C., Johnson, A.M., et al. (2025). Granzyme K+ CD8 T cells slow tauopathy progression by targeting microglia. Nat. Immunol. *26*, 1152–1167. https://doi.org/10.1038/s41590-025-02198-4.

25. Sulzer, D., Alcalay, R.N., Garretti, F., Cote, L., Kanter, E., Agin-Liebes, J., Liong, C., McMurtrey, C., Hildebrand, W.H., Mao, X., et al. (2017). T cells from patients with Parkinson's disease recognize alpha-synuclein peptides. Nature *546*, 656–661. https://doi.org/10.1038/nature22815.

26. Gate, D., Tapp, E., Leventhal, O., Shahid, M., Nonninger, T.J., Yang, A.C., Strempfl, K., Unger, M.S., Fehlmann, T., Oh, H., et al. (2021). CD4(+) T cells contribute to neurodegeneration in Lewy body dementia. Science *374*, 868–874. https://doi.org/10.1126/science.abf7266.

27. Gulen, M.F., Samson, N., Keller, A., Schwabenland, M., Liu, C., Glück, S., Thacker, V.V., Favre, L., Mangeat, B., Kroese, L.J., et al. (2023). cGAS-STING drives ageing-related inflammation and neurodegeneration. Nature *620*, 374–380. https://doi.org/10.1038/s41586-023-06373-1.

28. Kalamakis, G., Brüne, D., Ravichandran, S., Bolz, J., Fan, W., Ziebell, F., Stiehl, T., Catalá-Martinez, F., Kupke, J., Zhao, S., et al. (2019). Quiescence Modulates Stem Cell Maintenance and Regenerative Capacity in the Aging Brain. Cell *176*, 1407–1419.e14. https://doi.org/10.1016/j.cell.2019.01.040.

29. Hammond, T.R., Marsh, S.E., and Stevens, B. (2019). Immune Signaling in Neurodegeneration. Immunity *50*, 955–974. https://doi.org/10.1016/j.immuni.2019.03.016.

30. Lemaitre, P., Tareen, S.H., Pasciuto, E., Mascali, L., Martirosyan, A., Callaerts-Vegh, Z., Poovathingal, S., Dooley, J., Holt, M.G., Yshii, L., et al. (2023). Molecular and cognitive signatures of ageing partially restored through synthetic delivery of IL2 to the brain. EMBO Mol. Med. *15*, e16805. https://doi.org/10.15252/emmm.202216805.

31. Furman, D., Campisi, J., Verdin, E., Carrera-Bastos, P., Targ, S., Franceschi, C., Ferrucci, L., Gilroy, D.W., Fasano, A., Miller, G.W., et al. (2019). Chronic inflammation in the etiology of disease across the life span. Nat. Med. *25*, 1822–1832. https://doi.org/10.1038/s41591-019-0675-0.

32. Keren-Shaul, H., Spinrad, A., Weiner, A., Matcovitch-Natan, O., Dvir-Szternfeld, R., Ulland, T.K., David, E., Baruch, K., Lara-Astaiso, D., Toth, B., et al. (2017). A Unique Microglia Type Associated with Restricting Development of Alzheimer's Disease. Cell *169*, 1276–1290.e17. https://doi.org/10.1016/j.cell.2017.05.018.

33. Mathys, H., Davila-Velderrain, J., Peng, Z., Gao, F., Mohammadi, S., Young, J.Z., Menon, M., He, L., Abdurrob, F., Jiang, X., et al. (2019). Single-cell transcriptomic analysis of Alzheimer's disease. Nature *570*, 332–337. https://doi.org/10.1038/s41586-019-1195-2.

34. Martins-Ferreira, R., Calafell-Segura, J., Leal, B., Rodríguez-Ubreva, J., Martínez-Saez, E., Mereu, E., Pinho E Costa, P., Laguna, A., and Ballestar, E. (2025). The Human Microglia Atlas (HuMicA) unravels changes in disease-associated microglia subsets across neurodegenerative conditions. Nat. Commun. *16*, 739. https://doi.org/10.1038/s41467-025-56124-1.

35. Hammond, T.R., Dufort, C., Dissing-Olesen, L., Giera, S., Young, A., Wysoker, A., Walker, A.J., Gergits, F., Segel, M., Nemesh, J., et al. (2019). Single-Cell RNA Sequencing of Microglia throughout the Mouse Lifespan and in the Injured Brain Reveals Complex Cell-State Changes. Immunity *50*, 253–271.e6. https://doi.org/10.1016/j.immuni.2018.11.004.

36. Carvajal Ibañez, D., Skabkin, M., Hooli, J., Cerrizuela, S., Göpferich, M., Jolly, A., Volk, K., Zumwinkel, M., Bertolini, M., Figlia, G., et al. (2023). Interferon regulates neural stem cell function at all ages by orchestrating mTOR and cell cycle. EMBO Mol. Med. *15*, e16434. https://doi.org/10.15252/emmm.202216434.

37. Ito, M., Komai, K., Mise-Omata, S., Iizuka-Koga, M., Noguchi, Y., Kondo, T., Sakai, R., Matsuo, K., Nakayama, T., Yoshie, O., et al. (2019). Brain regulatory T cells suppress astrogliosis and potentiate neurological recovery. Nature *565*, 246–250. https://doi.org/10.1038/s41586-018-0824-5.

38. Jin, W.N., Shi, K., He, W., Sun, J.H., Van Kaer, L., Shi, F.D., and Liu, Q. (2021). Neuroblast senescence in the aged brain augments natural killer cell cytotoxicity leading to impaired neurogenesis and cognition. Nat. Neurosci. *24*, 61–73. https://doi.org/10.1038/s41593-020-00745-w.

39. Baruch, K., Deczkowska, A., David, E., Castellano, J.M., Miller, O., Kertser, A., Berkutzki, T., Barnett-Itzhaki, Z., Bezalel, D., Wyss-Coray, T., et al. (2014). Aging. Aging-induced type I interferon response at the choroid plexus negatively affects brain function. Science *346*, 89–93. https://doi.org/10.1126/science.1252945.

40. Vinnakota, J.M., Adams, R.C., Athanassopoulos, D., Schmidt, D., Biavasco, F., Zähringer, A., Erny, D., Schwabenland, M., Langenbach, M., Wenger, V., et al. (2024). Anti-PD-1 cancer immunotherapy induces central nervous system immune-related adverse events by microglia activation. Sci. Transl. Med. *16*, eadj9672. https://doi.org/10.1126/scitranslmed.adj9672.

41. Baruch, K., Deczkowska, A., Rosenzweig, N., Tsitsou-Kampeli, A., Sharif, A.M., Matcovitch-Natan, O., Kertser, A., David, E., Amit, I., and Schwartz, M. (2016). PD-1 immune checkpoint blockade reduces pathology and improves memory in mouse models of Alzheimer's disease. Nat. Med. *22*, 135–137. https://doi.org/10.1038/nm.4022.

42. Deczkowska, A., Matcovitch-Natan, O., Tsitsou-Kampeli, A., Ben-Hamo, S., Dvir-Szternfeld, R., Spinrad, A., Singer, O., David, E., Winter, D.R., Smith, L.K., et al. (2017). Mef2C restrains microglial inflammatory response and is lost in brain ageing in an IFN-I-dependent manner. Nat. Commun. *8*, 717. https://doi.org/10.1038/s41467-017-00769-0.

43. Gao, W., Kim, M.W., Dykstra, T., Du, S., Boskovic, P., Lichti, C.F., Ruiz-Cardozo, M.A., Gu, X., Weizman Shapira, T., Rustenhoven, J., et al. (2024). Engineered T cell therapy for central nervous system injury. Nature *634*, 693–701. https://doi.org/10.1038/s41586-024-07906-y.

44. Rosenzweig, N., Dvir-Szternfeld, R., Tsitsou-Kampeli, A., Keren-Shaul, H., Ben-Yehuda, H., Weill-Raynal, P., Cahalon, L., Kertser, A., Baruch, K., Amit, I., et al. (2019). PD-1/PD-L1 checkpoint blockade harnesses monocyte-derived macrophages to combat cognitive impairment in a tauopathy mouse model. Nat. Commun. *10*, 465. https://doi.org/10.1038/s41467-019-08352-5.

45. Sanchez-Molina, P., Almolda, B., Giménez-Llort, L., González, B., and Castellano, B. (2022). Chronic IL-10 overproduction disrupts microglia-neuron dialogue similar to aging, resulting in impaired hippocampal neurogenesis and spatial memory. Brain Behav. Immun. *101*, 231–245. https://doi.org/10.1016/j.bbi.2021.12.026.

46. Bond, A.M., Ming, G.L., and Song, H. (2015). Adult Mammalian Neural Stem Cells and Neurogenesis: Five Decades Later. Cell Stem Cell *17*, 385–395. https://doi.org/10.1016/j.stem.2015.09.003.

47. McAvoy, K.M., Scobie, K.N., Berger, S., Russo, C., Guo, N., Decharatanachart, P., Vega-Ramirez, H., Miake-Lye, S., Whalen, M., Nelson, M., et al. (2016). Modulating Neuronal Competition Dynamics in the Dentate Gyrus to Rejuvenate Aging Memory Circuits. Neuron *91*, 1356–1373. https://doi.org/10.1016/j.neuron.2016.08.009.

48. Navarro Negredo, P., Yeo, R.W., and Brunet, A. (2020). Aging and Rejuvenation of Neural Stem Cells and Their Niches. Cell Stem Cell *27*, 202–223. https://doi.org/10.1016/j.stem.2020.07.002.

49. Zhou, Y., Su, Y., Li, S., Kennedy, B.C., Zhang, D.Y., Bond, A.M., Sun, Y., Jacob, F., Lu, L., Hu, P., et al. (2022). Molecular landscapes of human hippocampal immature neurons across lifespan. Nature *607*, 527–533. https://doi.org/10.1038/s41586-022-04912-w.

50. Liu, L., Kim, S., Buckley, M.T., Reyes, J.M., Kang, J., Tian, L., Wang, M., Lieu, A., Mao, M., Rodriguez-Mateo, C., et al. (2023). Exercise reprograms the inflammatory landscape of multiple stem cell compartments during mammalian aging. Cell Stem Cell *30*, 689–705.e4. https://doi.org/10.1016/j.stem.2023.03.016.

51. Mogilenko, D.A., Shpynov, O., Andhey, P.S., Arthur, L., Swain, A., Esaulova, E., Brioschi, S., Shchukina, I., Kerndl, M., Bambouskova, M., et al. (2021). Comprehensive Profiling of an Aging Immune System Reveals Clonal GZMK+ CD8+ T Cells as Conserved Hallmark of Inflammaging. Immunity *54*, 99–115.e12. https://doi.org/10.1016/j.immuni.2020.11.005.

52. Terekhova, M., Swain, A., Bohacova, P., Aladyeva, E., Arthur, L., Laha, A., Mogilenko, D.A., Burdess, S., Sukhov, V., Kleverov, D., et al. (2023). Single-cell atlas of healthy human blood unveils age-related loss of NKG2C(+)GZMB(-)CD8(+) memory T cells and accumulation of type 2 memory T cells. Immunity *56*, 2836–2854.e9. https://doi.org/10.1016/j.immuni.2023.10.013.

53. Marschallinger, J., Iram, T., Zardeneta, M., Lee, S.E., Lehallier, B., Haney, M.S., Pluvinage, J.V., Mathur, V., Hahn, O., Morgens, D.W., et al. (2020). Lipid-droplet-accumulating microglia represent a dysfunctional and proinflammatory state in the aging brain. Nat. Neurosci. *23*, 194–208. https://doi.org/10.1038/s41593-019-0566-1.

54. Paolicelli, R.C., Sierra, A., Stevens, B., Tremblay, M.E., Aguzzi, A., Ajami, B., Amit, I., Audinat, E., Bechmann, I., Bennett, M., et al. (2022). Microglia states and nomenclature: A field at its crossroads. Neuron *110*, 3458–3483. https://doi.org/10.1016/j.neuron.2022.10.020.

55. Sierra, A., Gottfried-Blackmore, A.C., McEwen, B.S., and Bulloch, K. (2007). Microglia derived from aging mice exhibit an altered inflammatory profile. Glia *55*, 412–424. https://doi.org/10.1002/glia.20468.

56. Solano Fonseca, R., Mahesula, S., Apple, D.M., Raghunathan, R., Dugan, A., Cardona, A., O'Connor, J., and Kokovay, E. (2016). Neurogenic Niche Microglia Undergo Positional Remodeling and Progressive Activation Contributing to Age-Associated Reductions in Neurogenesis. Stem Cells Dev. *25*, 542–555. https://doi.org/10.1089/scd.2015.0319.

57. Scott-Hewitt, N., Mahoney, M., Huang, Y., Korte, N., Yvanka de Soysa, T., Wilton, D.K., Knorr, E., Mastro, K., Chang, A., Zhang, A., et al. (2024). Microglial-derived C1q integrates into neuronal ribonucleoprotein

complexes and impacts protein homeostasis in the aging brain. Cell *187*, 4193–4212.e24. https://doi.org/10.1016/j.cell.2024.05.058.

58. Buckley, M.T., Sun, E.D., George, B.M., Liu, L., Schaum, N., Xu, L., Reyes, J.M., Goodell, M.A., Weissman, I.L., Wyss-Coray, T., et al. (2023). Cell-type-specific aging clocks to quantify aging and rejuvenation in neurogenic regions of the brain. Nat Aging *3*, 121–137. https://doi.org/10.1038/s43587-022-00335-4.

59. Saraiva, M., Vieira, P., and O'Garra, A. (2020). Biology and therapeutic potential of interleukin-10. J. Exp. Med. *217*, e20190418. https://doi.org/10.1084/jem.20190418.

60. Saxton, R.A., Tsutsumi, N., Su, L.L., Abhiraman, G.C., Mohan, K., Henneberg, L.T., Aduri, N.G., Gati, C., and Garcia, K.C. (2021). Structure-based decoupling of the pro- and anti-inflammatory functions of interleukin-10. Science *371*, eabc8433. https://doi.org/10.1126/science.abc8433.

61. Ouyang, W., and O'Garra, A. (2019). IL-10 Family Cytokines IL-10 and IL-22: from Basic Science to Clinical Translation. Immunity *50*, 871–891. https://doi.org/10.1016/j.immuni.2019.03.020.

62. Chamoto, K., Yaguchi, T., Tajima, M., and Honjo, T. (2023). Insights from a 30-year journey: function, regulation and therapeutic modulation of PD1. Nat. Rev. Immunol. *23*, 682–695. https://doi.org/10.1038/s41577-023-00867-9.

63. Gong, J., Chehrazi-Raffle, A., Reddi, S., and Salgia, R. (2018). Development of PD-1 and PD-L1 inhibitors as a form of cancer immunotherapy: a comprehensive review of registration trials and future considerations. J. Immunother. Cancer *6*, 8. https://doi.org/10.1186/s40425-018-0316-z.

64. Leach, D.R., Krummel, M.F., and Allison, J.P. (1996). Enhancement of antitumor immunity by CTLA-4 blockade. Science *271*, 1734–1736. https://doi.org/10.1126/science.271.5256.1734.

65. Nishimura, H., Minato, N., Nakano, T., and Honjo, T. (1998). Immunological studies on PD-1 deficient mice: implication of PD-1 as a negative regulator for B cell responses. Int. Immunol. *10*, 1563–1572. https://doi.org/10.1093/intimm/10.10.1563.

66. Wei, S.C., Duffy, C.R., and Allison, J.P. (2018). Fundamental Mechanisms of Immune Checkpoint Blockade Therapy. Cancer Discov. *8*, 1069–1086. https://doi.org/10.1158/2159-8290.CD-18-0367.

67. Sharma, P., and Allison, J.P. (2015). Immune checkpoint targeting in cancer therapy: toward combination strategies with curative potential. Cell *161*, 205–214. https://doi.org/10.1016/j.cell.2015.03.030.

68. Fernandes, R.A., Su, L., Nishiga, Y., Ren, J., Bhuiyan, A.M., Cheng, N., Kuo, C.J., Picton, L.K., Ohtsuki, S., Majzner, R.G., et al. (2020). Immune receptor inhibition through enforced phosphatase recruitment. Nature *586*, 779–784. https://doi.org/10.1038/s41586-020-2851-2.

69. Doetsch, F., Caillé, I., Lim, D.A., García-Verdugo, J.M., and Alvarez-Buylla, A. (1999). Subventricular zone astrocytes are neural stem cells in the adult mammalian brain. Cell *97*, 703–716. https://doi.org/10.1016/s0092-8674(00)80783-7.

70. Doetsch, F., Petreanu, L., Caille, I., Garcia-Verdugo, J.M., and Alvarez-Buylla, A. (2002). EGF converts transit-amplifying neurogenic precursors in the adult brain into multipotent stem cells. Neuron *36*, 1021–1034. https://doi.org/10.1016/s0896-6273(02)01133-9.

71. Kjell, J., Fischer-Sternjak, J., Thompson, A.J., Friess, C., Sticco, M.J., Salinas, F., Cox, J., Martinelli, D.C., Ninkovic, J., Franze, K., et al. (2020). Defining the Adult Neural Stem Cell Niche Proteome Identifies Key Regulators of Adult Neurogenesis. Cell Stem Cell *26*, 277–293.e8. https://doi.org/10.1016/j.stem.2020.01.002.

72. Perez-Asensio, F.J., Perpiñá, U., Planas, A.M., and Pozas, E. (2013). Interleukin-10 regulates progenitor differentiation and modulates neurogenesis in adult brain. J. Cell Sci. *126*, 4208–4219. https://doi.org/10.1242/jcs.127803.

73. Silva-Vargas, V., Maldonado-Soto, A.R., Mizrak, D., Codega, P., and Doetsch, F. (2016). Age-Dependent Niche Signals from the Choroid Plexus Regulate Adult Neural Stem Cells. Cell Stem Cell *19*, 643–652. https://doi.org/10.1016/j.stem.2016.06.013.

74. DeVos, S.L., and Miller, T.M. (2013). Direct intraventricular delivery of drugs to the rodent central nervous system. J. Vis. Exp. *75*, e50326. https://doi.org/10.3791/50326.

75. Xu, L., Ramirez-Matias, J., Hauptschein, M., Sun, E.D., Lunger, J.C., Buckley, M.T., and Brunet, A. (2024). Restoration of neuronal progenitors by partial reprogramming in the aged neurogenic niche. Nat Aging *4*, 546–567. https://doi.org/10.1038/s43587-024-00594-3.

76. Li, G., Peskind, E.R., Millard, S.P., Chi, P., Sokal, I., Yu, C.E., Bekris, L.M., Raskind, M.A., Galasko, D.R., and Montine, T.J. (2009). Cerebrospinal fluid concentration of brain-derived neurotrophic factor and cognitive function in non-demented subjects. PLOS One *4*, e5424. https://doi.org/10.1371/journal.pone.0005424.

77. Chan, I.H., Wu, V., Bilardello, M., Mar, E., Oft, M., Van Vlasselaer, P., and Mumm, J.B. (2015). The Potentiation of IFN-gamma and Induction of Cytotoxic Proteins by Pegylated IL-10 in Human CD8 T Cells. J. Interferon Cytokine Res. *35*, 948–955. https://doi.org/10.1089/jir.2014.0221.

78. Fujii, S., Shimizu, K., Shimizu, T., and Lotze, M.T. (2001). Interleukin-10 promotes the maintenance of antitumor CD8(+) T-cell effector function in situ. Blood *98*, 2143–2151. https://doi.org/10.1182/blood.v98.7.2143.

79. Mumm, J.B., Emmerich, J., Zhang, X., Chan, I., Wu, L., Mauze, S., Blaisdell, S., Basham, B., Dai, J., Grein, J., et al. (2011). IL-10 elicits IFNgamma-dependent tumor immune surveillance. Cancer Cell *20*, 781–796. https://doi.org/10.1016/j.ccr.2011.11.003.

80. Yogev, N., Bedke, T., Kobayashi, Y., Brockmann, L., Lukas, D., Regen, T., Croxford, A.L., Nikolav, A., Hövelmeyer, N., von Stebut, E., et al. (2022). CD4+ T-cell-derived IL-10 promotes CNS inflammation in mice by sustaining effector T cell survival. Cell Rep. *38*, 110565. https://doi.org/10.1016/j.celrep.2022.110565.

81. Silva-Vargas, V., Crouch, E.E., and Doetsch, F. (2013). Adult neural stem cells and their niche: a dynamic duo during homeostasis, regeneration, and aging. Curr. Opin. Neurobiol. *23*, 935–942. https://doi.org/10.1016/j.conb.2013.09.004.

82. Nolte, E.D., Nolte, K.A., and Yan, S.S. (2019). Anxiety and task performance changes in an aging mouse model. Biochem. Biophys. Res. Commun. *514*, 246–251. https://doi.org/10.1016/j.bbrc.2019.04.049.

83. Xiong, X.D., Xiong, W.D., Xiong, S.S., and Chen, G.H. (2018). Age- and Gender-Based Differences in Nest-Building Behavior and Learning and Memory Performance Measured Using a Radial Six-Armed Water Maze in C57BL/6 Mice. Behav. Neurol. *2018*, 8728415. https://doi.org/10.1155/2018/8728415.

84. Minhas, P.S., Latif-Hernandez, A., McReynolds, M.R., Durairaj, A.S., Wang, Q., Rubin, A., Joshi, A.U., He, J.Q., Gauba, E., Liu, L., et al. (2021). Restoring metabolism of myeloid cells reverses cognitive decline in ageing. Nature *590*, 122–128. https://doi.org/10.1038/s41586-020-03160-0.

85. Pluvinage, J.V., Haney, M.S., Smith, B.A.H., Sun, J., Iram, T., Bonanno, L., Li, L., Lee, D.P., Morgens, D.W., Yang, A.C., et al. (2019). CD22 blockade restores homeostatic microglial phagocytosis in ageing brains. Nature *568*, 187–192. https://doi.org/10.1038/s41586-019-1088-4.

86. Ron-Harel, N., Segev, Y., Lewitus, G.M., Cardon, M., Ziv, Y., Netanely, D., Jacob-Hirsch, J., Amariglio, N., Rechavi, G., Domany, E., et al. (2008). Age-dependent spatial memory loss can be partially restored by immune activation. Rejuvenation Res. *11*, 903–913. https://doi.org/10.1089/rej.2008.0755.

87. Schroer, A.B., Ventura, P.B., Sucharov, J., Misra, R., Chui, M.K.K., Bieri, G., Horowitz, A.M., Smith, L.K., Encabo, K., Tenggara, I., et al. (2023). Platelet factors attenuate inflammation and rescue cognition in ageing. Nature *620*, 1071–1079. https://doi.org/10.1038/s41586-023-06436-3.

88. Shi, Q., Colodner, K.J., Matousek, S.B., Merry, K., Hong, S., Kenison, J.E., Frost, J.L., Le, K.X., Li, S., Dodart, J.C., et al. (2015). Complement C3-Deficient Mice Fail to Display Age-Related Hippocampal Decline.

J. Neurosci. *35*, 13029–13042. https://doi.org/10.1523/JNEUROSCI.1698-15.2015.

89. Kraeuter, A.K., Guest, P.C., and Sarnyai, Z. (2019). The Y-Maze for Assessment of Spatial Working and Reference Memory in Mice. Methods Mol. Biol. *1916*, 105–111. https://doi.org/10.1007/978-1-4939-8994-2_10.
90. Lueptow, L.M. (2017). Novel Object Recognition Test for the Investigation of Learning and Memory in Mice. J. Vis. Exp. *126*, 55718. https://doi.org/10.3791/55718.
91. Wang, T.W., Johmura, Y., Suzuki, N., Omori, S., Migita, T., Yamaguchi, K., Hatakeyama, S., Yamazaki, S., Shimizu, E., Imoto, S., et al. (2022). Blocking PD-L1-PD-1 improves senescence surveillance and ageing phenotypes. Nature *611*, 358–364. https://doi.org/10.1038/s41586-022-05388-4.
92. Damo, M., Hornick, N.I., Venkat, A., William, I., Clulo, K., Venkatesan, S., He, J., Fagerberg, E., Loza, J.L., Kwok, D., et al. (2023). PD-1 maintains CD8 T cell tolerance towards cutaneous neoantigens. Nature *619*, 151–159. https://doi.org/10.1038/s41586-023-06217-y.
93. Marin-Rodero, M., Cintado, E., Walker, A.J., Jayewickreme, T., Pinho-Ribeiro, F.A., Richardson, Q., Jackson, R., Chiu, I.M., Benoist, C., Stevens, B., et al. (2025). The meninges host a distinct compartment of regulatory T cells that preserves brain homeostasis. Sci. Immunol. *10*, eadu2910. https://doi.org/10.1126/sciimmunol.adu2910.
94. Castellani, G., Croese, T., Peralta Ramos, J.M., and Schwartz, M. (2023). Transforming the understanding of brain immunity. Science *380*, eabo7649. https://doi.org/10.1126/science.abo7649.
95. Da Mesquita, S., Louveau, A., Vaccari, A., Smirnov, I., Cornelison, R.C., Kingsmore, K.M., Contarino, C., Onengut-Gumuscu, S., Farber, E., Raper, D., et al. (2018). Functional aspects of meningeal lymphatics in ageing and Alzheimer's disease. Nature *560*, 185–191. https://doi.org/10.1038/s41586-018-0368-8.
96. Fitzpatrick, Z., Ghabdan Zanluqui, N., Rosenblum, J.S., Tuong, Z.K., Lee, C.Y.C., Chandrashekhar, V., Negro-Demontel, M.L., Stewart, A.P., Posner, D.A., Buckley, M., et al. (2024). Venous-plexus-associated lymphoid hubs support meningeal humoral immunity. Nature *628*, 612–619. https://doi.org/10.1038/s41586-024-07202-9.
97. Louveau, A., Smirnov, I., Keyes, T.J., Eccles, J.D., Rouhani, S.J., Peske, J.D., Derecki, N.C., Castle, D., Mandell, J.W., Lee, K.S., et al. (2015). Structural and functional features of central nervous system lymphatic vessels. Nature *523*, 337–341. https://doi.org/10.1038/nature14432.
98. Mrdjen, D., Pavlovic, A., Hartmann, F.J., Schreiner, B., Utz, S.G., Leung, B.P., Lelios, I., Heppner, F.L., Kipnis, J., Merkler, D., et al. (2018). High-Dimensional Single-Cell Mapping of Central Nervous System Immune Cells Reveals Distinct Myeloid Subsets in Health, Aging, and Disease. Immunity *48*, 599. https://doi.org/10.1016/j.immuni.2018.02.014.
99. Rustenhoven, J., Drieu, A., Mamuladze, T., de Lima, K.A., Dykstra, T., Wall, M., Papadopoulos, Z., Kanamori, M., Salvador, A.F., Baker, W., et al. (2021). Functional characterization of the dural sinuses as a neuroimmune interface. Cell *184*, 1000–1016.e27. https://doi.org/10.1016/j.cell.2020.12.040.
100. Zhang, Y., Bailey, J.T., Xu, E., Singh, K., Lavaert, M., Link, V.M., D'Souza, S., Hafiz, A., Cao, J., Cao, G., et al. (2022). Mucosal-associated invariant T cells restrict reactive oxidative damage and preserve meningeal barrier integrity and cognitive function. Nat. Immunol. *23*, 1714–1725. https://doi.org/10.1038/s41590-022-01349-1.
101. Kim, M.W., and Kipnis, J. (2025). Glymphatics and meningeal lymphatics unlock the brain-immune code. Immunity *58*, 1040–1051. https://doi.org/10.1016/j.immuni.2025.03.006.
102. Yoshida, T.M., Nguyen, M., Zhang, L., Lu, B.Y., Zhu, B., Murray, K.N., Mineur, Y.S., Zhang, C., Xu, D., Lin, E., et al. (2025). The subfornical organ is a nucleus for gut-derived T cells that regulate behaviour. Nature *643*, 499–508. https://doi.org/10.1038/s41586-025-09050-7.
103. Boissonneault, V., Filali, M., Lessard, M., Relton, J., Wong, G., and Rivest, S. (2009). Powerful beneficial effects of macrophage colony-stimulating factor on beta-amyloid deposition and cognitive impairment in Alzheimer's disease. Brain *132*, 1078–1092. https://doi.org/10.1093/brain/awn331.
104. Kiyota, T., Ingraham, K.L., Swan, R.J., Jacobsen, M.T., Andrews, S.J., and Ikezu, T. (2012). AAV serotype 2/1-mediated gene delivery of anti-inflammatory interleukin-10 enhances neurogenesis and cognitive function in APP+PS1 mice. Gene Ther. *19*, 724–733. https://doi.org/10.1038/gt.2011.126.
105. Lobo-Silva, D., Carriche, G.M., Castro, A.G., Roque, S., and Saraiva, M. (2016). Balancing the immune response in the brain: IL-10 and its regulation. J. Neuroinflamm. *13*, 297. https://doi.org/10.1186/s12974-016-0763-8.
106. Weston, L.L., Jiang, S., Chisholm, D., Jantzie, L.L., and Bhaskar, K. (2021). Interleukin-10 deficiency exacerbates inflammation-induced tau pathology. J. Neuroinflamm. *18*, 161. https://doi.org/10.1186/s12974-021-02211-1.
107. Chakrabarty, P., Li, A., Ceballos-Diaz, C., Eddy, J.A., Funk, C.C., Moore, B., DiNunno, N., Rosario, A.M., Cruz, P.E., Verbeeck, C., et al. (2015). IL-10 alters immunoproteostasis in APP mice, increasing plaque burden and worsening cognitive behavior. Neuron *85*, 519–533. https://doi.org/10.1016/j.neuron.2014.11.020.
108. Guillot-Sestier, M.V., Doty, K.R., Gate, D., Rodriguez, J., Jr., Leung, B.P., Rezai-Zadeh, K., and Town, T. (2015). Il10 deficiency rebalances innate immunity to mitigate Alzheimer-like pathology. Neuron *85*, 534–548. https://doi.org/10.1016/j.neuron.2014.12.068.
109. Ross, J.B., Myers, L.M., Noh, J.J., Collins, M.M., Carmody, A.B., Messer, R.J., Dhuey, E., Hasenkrug, K.J., and Weissman, I.L. (2024). Depleting myeloid-biased haematopoietic stem cells rejuvenates aged immunity. Nature *628*, 162–170. https://doi.org/10.1038/s41586-024-07238-x.
110. Gabandé-Rodríguez, E., Soto-Heredero, G., Carrasco, E., Anerillas, C., Escrig-Larena, J.I., Delgado-Pulido, S., Francos-Quijorna, I., Gómez de las Heras, M.M., Fernández-Almeida, Á., Blanco, E.M., et al. (2024). Cytotoxic CD4+ T cells in the bone marrow compromise healthy ageing by enhancing granulopoiesis. Preprint at bioRxiv. https://doi.org/10.1101/2024.01.26.577360.
111. Campisi, J., Kapahi, P., Lithgow, G.J., Melov, S., Newman, J.C., and Verdin, E. (2019). From discoveries in ageing research to therapeutics for healthy ageing. Nature *571*, 183–192. https://doi.org/10.1038/s41586-019-1365-2.
112. Gabandé-Rodríguez, E., Pfeiffer, M., and Mittelbrunn, M. (2023). Immuno(T)herapy for age-related diseases. EMBO Mol. Med. *15*, e16301. https://doi.org/10.15252/emmm.202216301.
113. Saura, J., Tusell, J.M., and Serratosa, J. (2003). High-yield isolation of murine microglia by mild trypsinization. Glia *44*, 183–189. https://doi.org/10.1002/glia.10274.
114. Tsai, A.P., Dong, C., Lin, P.B.C., Oblak, A.L., Viana Di Prisco, G., Wang, N., Hajicek, N., Carr, A.J., Lendy, E.K., Hahn, O., et al. (2023). Genetic variants of phospholipase C-gamma2 alter the phenotype and function of microglia and confer differential risk for Alzheimer's disease. Immunity *56*, 2121–2136.e6. https://doi.org/10.1016/j.immuni.2023.08.008.
115. Rossotti, M., Tabares, S., Alfaya, L., Leizagoyen, C., Moron, G., and González-Sapienza, G. (2015). Streamlined method for parallel identification of single domain antibodies to membrane receptors on whole cells. Biochim. Biophys. Acta *1850*, 1397–1404. https://doi.org/10.1016/j.bbagen.2015.03.009.
116. Zhao, P., Wang, P., Dong, S., Zhou, Z., Cao, Y., Yagita, H., He, X., Zheng, S.G., Fisher, S.J., Fujinami, R.S., et al. (2019). Depletion of PD-1-positive cells ameliorates autoimmune disease. Nat. Biomed. Eng. *3*, 292–305. https://doi.org/10.1038/s41551-019-0360-0.
117. Yeo, R.W., Zhou, O.Y., Zhong, B.L., Sun, E.D., Navarro Negredo, P., Nair, S., Sharmin, M., Ruetz, T.J., Wilson, M., Kundaje, A., et al. (2023). Chromatin accessibility dynamics of neurogenic niche cells reveal defects in neural stem cell adhesion and migration during aging. Nat Aging *3*, 866–893. https://doi.org/10.1038/s43587-023-00449-3.

118. Iram, T., Kern, F., Kaur, A., Myneni, S., Morningstar, A.R., Shin, H., Garcia, M.A., Yerra, L., Palovics, R., Yang, A.C., et al. (2022). Young CSF restores oligodendrogenesis and memory in aged mice via Fgf17. Nature *605*, 509–515. https://doi.org/10.1038/s41586-022-04722-0.

119. Korsunsky, I., Millard, N., Fan, J., Slowikowski, K., Zhang, F., Wei, K., Baglaenko, Y., Brenner, M., Loh, P.R., and Raychaudhuri, S. (2019). Fast, sensitive and accurate integration of single-cell data with Harmony. Nat. Methods *16*, 1289–1296. https://doi.org/10.1038/s41592-019-0619-0.

120. Andreatta, M., and Carmona, S.J. (2021). UCell: Robust and scalable single-cell gene signature scoring. Comput. Struct. Biotechnol. J. *19*, 3796–3798. https://doi.org/10.1016/j.csbj.2021.06.043.

121. Wolock, S.L., Lopez, R., and Klein, A.M. (2019). Scrublet: Computational Identification of Cell Doublets in Single-Cell Transcriptomic Data. Cell Syst. *8*, 281–291.e9. https://doi.org/10.1016/j.cels.2018.11.005.

122. Deacon, R.M.J. (2006). Assessing nest building in mice. Nat. Protoc. *1*, 1117–1119. https://doi.org/10.1038/nprot.2006.170.

STAR★METHODS

KEY RESOURCES TABLE

REAGENT or RESOURCE	SOURCE	IDENTIFIER
Antibodies		
Purified anti-mouse CD3ε Antibody	BioLegend	Cat# 100302; RRID: AB_312667
Purified anti-mouse CD28 Antibody	BioLegend	Cat# 102102; RRID: AB_312867
InVivoMAb anti-mouse PD-1 (CD279)	Bio X Cell	Cat# BE0146; RRID: AB_10949053
Alexa Fluor® 700 anti-mouse CD69 Antibody	BioLegend	Cat# 104539; RRID: AB_2566304
Brilliant Violet 605™ anti-mouse CD25 Antibody	BioLegend	Cat# 102036; RRID: AB_2563059
InVivoPlus rat IgG2a isotype control	Bio X Cell	Cat# BE0089; RRID: AB_1107769
Anti-mouse IFNAR-1-InVivo	Selleck	Cat# A2121; RRID: AB_2927720
Mouse IgG1 isotype control-InVivo	Selleck	Cat# A2106, RRID: AB_3722689
InVivoMAb anti-mouse IFNγ	Bio X Cell	Cat# BE0054; RRID: AB_1107692
Rat IgG1 isotype control-InVivo	Selleck	Cat# A2119; RRID: AB_3697767
PE anti-mouse CD45 Antibody	BioLegend	Cat# 103106; RRID: AB_312971
FITC anti-mouse CD8a Antibody	BioLegend	Cat# 100705; RRID: AB_312744
Brilliant Violet 785™ anti-mouse CD8a Antibody	BioLegend	Cat# 100750; RRID: AB_2562610
PerCP/Cyanine5.5 anti-mouse/human CD11b Antibody	BioLegend	Cat# 101227; RRID: AB_893233
Alexa Fluor® 700 anti-mouse CD3 Antibody	BioLegend	Cat# 100216; RRID: AB_493697
PerCP anti-mouse CD25 Antibody	BioLegend	Cat# 102027; RRID: AB_893290
FITC anti-mouse CD279 (PD-1) Antibody	BioLegend	Cat# 135213; RRID: AB_10689633
Brilliant Violet 711™ anti-mouse CD223 (LAG-3) Antibody	BioLegend	Cat# 125243; RRID: AB_2876450
Brilliant Violet 605™ anti-mouse/human CD44 Antibody	BioLegend	Cat# 103047; RRID: AB_2562451
CD69 Hamster anti-Mouse, BUV661, Clone: H1.2F3	BD Biosciences	Cat# 741478; RRID: AB_2870943
CD4 Rat anti-Murine, Brilliant Ultraviolet 496, Clone: GK1.5	BD Biosciences	Cat# 612952; RRID: AB_2813886
PE anti-mouse CD45 Antibody	BioLegend	Cat# 103106; RRID: AB_312971
FITC anti-mouse CD317 (BST2, PDCA-1) Antibody	BioLegend	Cat# 127007; RRID: AB_1953281
PE/Cyanine7 anti-mouse H-2Kd/H-2Dd Antibody	BioLegend	Cat# 114717; RRID: AB_2749955
FITC anti-mouse CD86 Antibody	BioLegend	Cat# 105005; RRID: AB_313148
TruStain FcX™ (anti-mouse CD16/32) Antibody	BioLegend	Cat# 101319; RRID: AB_1574973
PE anti-mouse CD45 Antibody	BioLegend	Cat# 103106; RRID: AB_312971
APC anti-mouse CD4 Antibody	BioLegend	Cat# 100412; RRID: AB_312697
BD Phosflow™ PE Mouse Anti-Stat3 (pY705)	BD Biosciences	Cat# 562072; RRID: AB_10893601
InVivoMAb rat IgG1 Isotype control, anti-trinitrophenol	Bio X Cell	Cat# BE0290; RRID: AB_2687813
PE anti-mouse CD317 (BST2, PDCA-1) Antibody	BioLegend	Cat# 127010; RRID: AB_1953285
PerCP anti-mouse/human CD11b Antibody	BioLegend	Cat# 101229; RRID: AB_2129375
Pacific Blue™ anti-mouse CD45 Antibody	BioLegend	Cat# 103125; RRID: AB_493536
Brilliant Violet 785™ anti-mouse CD8a Antibody	BioLegend	Cat# 100750; RRID: AB_2562610
FITC anti-mouse H-2K^{b}/H-2D^{b} Antibody	BioLegend	Cat# 114606; RRID: AB_313597
FITC anti-mouse CD317 (BST2, PDCA-1) Antibody	BioLegend	Cat# Cat# 127008; RRID: AB_2028462
APC anti-mouse CD8a Antibody	BioLegend	Cat# 100712; RRID: AB_312751
FITC anti-mouse CD8a Antibody	BioLegend	Cat# 100803; RRID: AB_312764
Rabbit monoclonal anti-CD3	Novus	Cat# NB600-1441; RRID: AB_789102
Rat monoclonal anti-CD68	BioLegend	Cat# 137001; RRID: AB_2044003
Rat monoclonal CD8α	Bio-Rad	Cat# MCA609GA; RRID: AB_323706
Rabbit polyclonal anti-doublecortin (DCX)	Cell Signaling Technology	Cat# 4604; RRID: AB_561007
Goat polyclonal anti-GFAP	Abcam	Cat# ab53554; RRID: AB_880202

(*Continued on next page*)

Continued

REAGENT or RESOURCE	SOURCE	IDENTIFIER
Goat polyclonal anti-IBA1	Novus	Cat# NB 100–1028; RRID: AB_521594
Rabbit polyclonal anti-fragilis (IFITM3)	Abcam	Cat# ab15592; RRID: AB_2122095
Rat monoclonal anti-Ki67	Thermo Fisher Scientific	Cat# 14-5698-82; RRID: AB_10854564
Mouse monoclonal anti-NeuN	Millipore	Cat# MAB377; RRID: AB_2298772
Goat polyclonal anti-OLIG2	R and D Systems	Cat# AF2418; RRID: AB_2157554
Goat polyclonal anti-PD1	R and D Systems	Cat# AF1021; RRID: AB_354541
Rabbit monoclonal anti-STAT1	Cell Signaling Technology	Cat# 14994; RRID: AB_2737027
Guinea pig polyclonal anti-TMEM119	Synaptic Systems	Cat# 400 004; RRID: AB_2744645
Donkey anti-Rabbit IgG (H+L) Highly Cross-Adsorbed Secondary Antibody, Alexa Fluor™ 568	Thermo Fisher Scientific	Cat# A10042; RRID: AB_2534017
Donkey anti-Rat IgG (H+L) Highly Cross-Adsorbed Secondary Antibody, Alexa Fluor™ 488	Thermo Fisher Scientific	Cat# A-21208; RRID: AB_2535794
Donkey anti-Goat IgG (H+L) Cross-Adsorbed Secondary Antibody, Alexa Fluor™ 647	Thermo Fisher Scientific	Cat# A-21447; RRID: AB_2535864
Chemicals, peptides, and recombinant proteins		
Mouse RIPR-PD1	Fernandes et al.[68]	N/A
Human RIPR-PD1	Fernandes et al.[68]	N/A
WT IL10	Saxton et al.[60]	N/A
IL-10 D25K variant	Saxton et al.[60]	N/A
Recombinant Mouse IL-2 Protein	R and D Systems	Cat# 402-ML-020/CF
Insect-XPRESS™ Protein-free Insect Cell Medium	Lonza	Cat# 12-730Q
Gentamycin Sulfate	Thermo Fisher Scientific	Cat# 613980010
Expi293™ Expression Medium	Thermo Fisher Scientific	Cat# A1435101
DMEM, high glucose	Thermo Fisher Scientific	Cat# 11965092
Fetal Bovine Serum	Millipore Sigma	Cat# F2442
Penicillin-Streptomycin-Glutamine (100X)	Thermo Fisher Scientific	Cat# 10378016
DMEM, high glucose, GlutaMAX™ Supplement	Thermo Fisher Scientific	Cat# 10566016
Advanced DMEM/F-12	Thermo Fisher Scientific	Cat# 12634028
GlutaMAX™ Supplement	Thermo Fisher Scientific	Cat# 35050061
Penicillin-Streptomycin (10,000 U/mL)	Thermo Fisher Scientific	Cat# 15140122
Trypsin-EDTA (0.25%), phenol red	Thermo Fisher Scientific	Cat# 25200056
RPMI 1640 Medium	Thermo Fisher Scientific	Cat# 11875093
MEM Non-Essential Amino Acids Solution (100X)	Thermo Fisher Scientific	Cat# 11140050
Sodium Pyruvate (100 mM)	Thermo Fisher Scientific	Cat# 11360070
HEPES (1M)	Thermo Fisher Scientific	Cat# 15-630-080
2-Mercaptoethanol	Thermo Fisher Scientific	Cat# 21-985-023
ACK Lysing Buffer	Thermo Fisher Scientific	Cat# A1049201
Ni-NTA Agarose	Qiagen	Cat# 30210
autoMACS® Running Buffer – MACS® Separation Buffer	Miltenyi Biotec	Cat# 130-091-221
Artificial Cerebrospinal Fluid	Tocris	Cat# 3525
2,2,2-Tribromoethanol	Sigma-Aldrich	Cat# T48402-25G
Corning™ Cell Culture Phosphate Buffered Saline (1X)	Corning	Cat# MT21040CV
Heparin sodium salt from porcine intestinal mucosa	Sigma-Aldrich	Cat# H3149-50KU
PIPES	Sigma-Aldrich	Cat# P1851
Papain	Worthington	Cat# LS003119
Trypsin inhibitor	Sigma-Aldrich	Cat# T9253
Deoxyribonuclease I from bovine pancreas	Sigma-Aldrich	Cat# DN25
DMEM/F-12, HEPES	Thermo Fisher Scientific	Cat# 11330032
Percoll®	Sigma-Aldrich	Cat# GE17-0891-01
D-(+)-Glucose	Sigma-Aldrich	Cat# G7021

(*Continued on next page*)

Continued

REAGENT or RESOURCE	SOURCE	IDENTIFIER
Propidium Iodide Solution	BioLegend	Cat# 421301
Collagenase, Type IV, powder	Thermo Fisher Scientific	Cat# 17104019
HBSS, calcium, magnesium, no phenol red	Thermo Fisher Scientific	Cat# 14025092
Paraformaldehyde 32% Aqueous Solution	Electron Microscopy Sciences	Cat# 15714
Sucrose	Sigma-Aldrich	Cat# S3929
O.C.T. Compound	Electron Microscopy Sciences	Cat# 62550-12
Triton™ X-100 (Electrophoresis), Fisher BioReagents™	Thermo Fisher Scientific	Cat# BP151
Trisodium citrate dihydrate	Sigma-Aldrich	Cat# S1804
TWEEN® 20	Sigma-Aldrich	Cat# P1379-1L
Normal Donkey Serum	ImmunoReagents	Cat# SP-072-VX10
Bovine Serum Albumin solution	Sigma-Aldrich	Cat# A7979
DAPI	Thermo Fisher Scientific	Cat# 62248
ProLong™ Gold Antifade Mountant with DNA Stain DAPI	Thermo Fisher Scientific	Cat# P36931
Poly-D-Lysine Hydrobromide	Sigma-Aldrich	Cat# P6407
Lipopolysaccharides from Escherichia coli O111:B4	Sigma-Aldrich	Cat# L2630
Methanol	Sigma-Aldrich	Cat# 34860
EDTA, 0.5M (pH 8.0), Molecular Grade, Promega™	Promega Corporation	Cat# PR-V4231
TrypLE™ Express Enzyme (1X), no phenol red	Thermo Fisher Scientific	Cat# 12604013
LIVE/DEAD™ Fixable Near-IR Dead Cell Stain Kit	Thermo Fisher Scientific	Cat# L10119
Zombie NIR™ Fixable Viability Kit	BioLegend	Cat# 423105
OneComp eBeads™ Compensation Beads	Thermo Fisher Scientific	Cat# 01-1111-41
Critical commercial assays		
Pierce Chromogenic Endotoxin Quant Kit	Thermo Fisher Scientific	Cat# A39552
CD8a+ T Cell Isolation Kit, mouse	Miltenyi Biotec	Cat# 130-104-075
ExpiFectamine 293 Transfection Kit	Thermo Fisher Scientific	Cat# A14525
Click-iT EdU Cell Proliferation Kit for Imaging, Alexa Fluor™ 488 dye	Thermo Fisher Scientific	Cat# C10337
Chromium Next GEM Single Cell 3′ Kit v3.1	10× Genomics	Cat# 1000123
Chromium Next GEM Single Cell 5′ v2 dual index kit	10× Genomics	Cat# 1000265
Dual Index Kit TT Set A	10× Genomics	Cat# 1000215
Library Construction Kit	10× Genomics	Cat# 1000157
Chromium Next GEM Chip G Single Cell Kit	10× Genomics	Cat# 1000127
ELISA MAX™ Deluxe Set Mouse IL-6	BioLegend	Cat# 431304
ELISA MAX™ Deluxe Set Mouse TNF-α	BioLegend	Cat# 430904
ELISA MAX™ Deluxe Set Mouse IFN-β	BioLegend	Cat# 439404
ELISA MAX™ Deluxe Set Mouse IFN-α1	BioLegend	Cat# 447904
Mouse Granzyme B DuoSet ELISA	R and D Systems	Cat# DY1865-05
Deposited data		
RNA-seq data generated in this study	This paper	BioProject PRJNA1365936
Code generated for analysis	This paper	Github: https://github.com/PalomaNavarro/TargetingImmuneCellsSVZ. Zenodo: https://doi.org/10.5281/zenodo.18174039
Experimental models: Cell lines		
Insect Tni cells	Expression Systems	Cat# 94-002S
Expi-293F cells	Thermo Fisher Scientific	Cat# A14527
BV2 microglia cells	Gift from Dr. Tony Wyss-Coray (Stanford University)	RRID: CVCL_0182
Experimental models: Organisms/strains		
C57BL/6J mice	National Institute on Aging	N/A
C57BL/6J mice	The Jackson Laboratory	Cat# 000664

(*Continued on next page*)

Continued

REAGENT or RESOURCE	SOURCE	IDENTIFIER
Software and algorithms		
NIS-Elements software (AR 4.30.02, 64-bit)	Nikon	https://www.microscope.healthcare.nikon.com/products/software/nis-elements
ZEN Blue 3.0 software	N/A	https://www.zeiss.com/microscopy/us/products/software/zeiss-zen.html
Fiji	ImageJ	https://imagej.net/software/fiji/downloads
FlowJo	Tree Star	https://www.flowjo.com/
Cell Ranger (version 3.0.2)	10x Genomics	https://www.10xgenomics.com/support/software/cell-ranger/latest
R (version 4.2.2)	R	https://www.r-project.org/
GraphPad Prism (version 10.2.0)	GraphPad	https://www.graphpad.com/features
SMART Video Tracking System (Panlab)	Harvard Apparatus	https://www.harvardapparatus.com/smart-video-tracking-system.html
Motor Monitor	Kinder Scientific	https://kinderscientific.com/software/motor-monitor/
BioRender	BioRender	https://www.biorender.com
Other		
BD FACSAria II Cell Sorter	BD Biosciences	RRID: SCR_018934
BD Symphony Flow Cytometer	BD Biosciences	RRDI: SCR_022674
BD LSRII Flow Cytometer	BD Biosciences	RRID: SCR_002159
CM3050 S Cryostat	Leica	RRID: SCR_016844
Zeiss LSM 900 confocal microscope	Zeiss	RRID: SCR_022263
Nikon Eclipse Ti microscope	Nikon	RRID: SCR_021242
Zyla sCMOS camera	Andor	RRID: SCR_023610
Enviro-dri® natural brown material	Shepherd Specialty Papers	N/A
ALZET Brain Infusion Kit 3	ALZET	Cat# 0008851
ALZET Mini osmotic pump 1007D	ALZET	Cat# 0000290
Small Animal Stereotaxic Instrument with Digital Display Console	Kopf	Model 940

EXPERIMENTAL MODEL AND STUDY PARTICIPANT DETAILS

Mice

All mice used in this study, except for primary microglia cultures, were C57BL/6 mice obtained from the National Institute on Aging (NIA) Aged Rodent colony with ages between 3 and 32 months. For primary microglia cultures, we used C57BL/6 mice from Jackson Laboratories. All mice used in this study were male mice (except for generation of primary microglia, which were performed on mixed sex mice). Mice were habituated for more than one week before use. At Stanford, all mice were housed in the Neuro-ChemH vivarium, and their care was monitored by the Veterinary Service Center at Stanford University under the Institutional Animal Care and Use Committee protocol 8661 and 29100. At UCSF, animals were housed at the UCSF Parnassus animal facility. Animals were moved to a new location for behavioral assessment at the Villeda Lab Behavioral Suite. All animal handling and use was in accordance with institutional guidelines approved by the University of California, San Francisco Institutional Animal Care and Use Committee (IACUC). All mice were housed under specific pathogen-free conditions with 12-hour light/dark cycles and ad libitum access to food and water in the cage.

Cell culture

Cells for protein production

Female insect Tni cells (Expression Systems, 94-002S) were grown in Insect X-press media (Lonza) with a final concentration of 10 mg/L of gentamicin sulfate (Thermo Fisher) at 27°C and atmospheric CO_2. Female Expi293F cells (Thermo, A14527) were grown in serum-free Expi293 expression media (Thermo, A1435101) and maintained at 37°C with 5% CO_2.

BV2 cell line

Female BV2 microglia cells were a kind gift from Tony Wyss-Coray (Stanford University) and were expanded in DMEM (Gibco, 11965092) supplemented with 10% fetal bovine serum (FBS, Millipore Sigma, F2442) and penicillin-streptomycin-glutamine (Gibco,

10378-016). BV2 cells were regularly tested for mycoplasma and were maintained in a humidified incubator containing 5% CO_2 at 37°C.

Mouse primary microglia

Primary microglia were isolated and cultured as previously described.[113,114] Briefly, brain tissue from C57BL/6 neonatal mice (both sexes) aged P2–P4 was homogenized in Dulbecco's Modified Eagle Medium (DMEM) (Gibco, 10566016) and sequentially filtered through 250 μm and 100 μm nylon meshes (Thermo, 1825505 and Falcon, 352320). The cell suspension was cultured in Advanced DMEM/F12 (Gibco 12634028) supplemented with 10% FBS, 1% GlutaMAX supplement (Gibco, 35050061) and Penicillin/Streptomycin (Gibco, 15140122). For FACS analysis, microglia were cultured in polystyrene 6-well plates (Falcon 08-772-1B). For immunofluorescence staining, microglia were cultured in a chamber slide system (Nunc Lab-Tek II Chamber Slide, 154453). After 21 days *in vitro*, mild trypsinization was performed using a 1:2 dilution of 0.25% EDTA-Trypsin (Gibco, 25200056) in DMEM for 20 minutes. The procedure selectively detached an intact layer of astrocytes and other glial cells, leaving microglia adherent to the bottom of the culture plate. The adherent microglia were used for experiments within 24 h. For experiments with RIPR-PD1, primary microglia were incubated with 1μM control or RIPR-PD1 for 48h and analyzed by FACS as explained below for co-culture experiments.

Primary mouse T cells

To isolate T cells for signaling assays and co-cultures, we removed the spleen and lymph nodes from middle-age to old male mice (12-29 months). We used the flat end of a syringe plunger to pass the spleen and lymph nodes through a 70 μm cell strainer. T cell media (RPMI 1640 with 10% FBS, 1% PSQ, 1% MEM non-essential amino acids (Gibco 11140-050), 1% GlutaMAX (Gibco 35050-061), 100 mM Sodium Pyruvate (Gibco 11360-070), 1M HEPES (Gibco 15-630-080), and 50μM 2-mercaptoethanol (Gibco 21985023)) was added to wash the cell strainer and the sample was centrifuged (3 min, 1200 rpm). For the spleen, we added 2 mL of ACK lysing buffer (Gibco, A1049201) to lyse red blood cells and incubated for 3 minutes at room temperature. After the lysis of red blood cells, 10 mL of T cell media was added and samples were spun for 3 min, 1200rpm. Spleen and lymph nodes extracts were pooled together and resuspended to 3 million cells per mL. To activate and expand T cells, 12 well plates that were coated overnight with anti-CD3 (BioLegend cat. no. 100302, Clone: 145-2C1 (2.5 μg/mL) were washed with PBS, and 1mL of a 2X T cell activating solution (T cell media, anti-CD28 (BioLegend cat. no. 102102, Clone: 37.51 (10 μg/mL) and recombinant mouse IL-2 (R&D Systems cat. no. 402-ML-020/CF (200 IU/mL)) was added to each well. Each well then received 3 million cells from the pooled spleen and lymph node cell suspension. T cells were incubated at 37°C for 48 hours. After this activation period, T cells were resuspended in T cell media without IL-2 and incubated at 37°C for 24 hours before use in experiments.

METHOD DETAILS

Engineered protein production and purification

RIPR-PD1

RIPR-PD1 is a hetero-bispecific diabody that binds to the CD45 and PD1 extracellular domains to compel cis-ligation of PD1 and CD45.[68] RIPR-PD1 induces cross-linking of PD1 to CD45 and inhibits both tonic and ligand-activated signaling through PD1 leading to enhanced inhibition of checkpoint blockade compared with ligand blocking by anti-PD1 antibodies.[68] While this molecule has not been tested in humans, it showed increased therapeutic efficacy over anti-PD1 antibodies in mouse models of small cell lung cancer and colon cancer.[68] Engineered checkpoint inhibitor proteins (RIPR-PD1 and control) were produced as previously described.[68] The mouse RIPR-PD1 is composed of a nanobody anti-CD45[115] fused to an anti-mouse PD-1 scFv, using the clone RMP1-14[116] using a GGGGTGGS or a GGSLEVLFQGPGSGS (3C) linker. The control for mouse RIPR-PD1 was human RIPR-PD1, which has a similar molecular weight but no ability to bind mouse PD1.[68] Human RIPR-PD1 is composed of the same anti-CD45 scFv as mouse RIPR-PD1 but fused to an anti-human PD-1 nanobody (VHH). Connecting the scFv to the VHH, a GGSLEVLFQGPGSGS linker sequence encoding a 3C cleavage site was used. All proteins were cloned in-frame in the pAc67-A (Pharmingen) plasmid for protein expression in Tni cells (BTI-Tn-5B1-4, Expression Systems, 94-002S) using the baculovirus expression system. Supernatant was harvested and used for protein purification 48-72 hours after infection with baculovirus. RIPR-PD1 molecules were purified by Ni-NTA (Qiagen) followed by size-exclusion chromatography using a Superdex 200 and PBS. Final endotoxin concentrations were determined using a chromogenic endotoxin quantitation kit (Thermo Scientific, A39552) and were never greater than 1 endotoxin unit per mg of purified protein.

Functional testing of RIPR-PD1

Purified mouse $CD8^+$ T cells (Milteny, 130-104-075) were stimulated as explained above. Mouse RIPR-PD1, control human RIPR-PD1, or anti-PD-1 antibody (BioXCell, clone RMP1-14, BE0146) were added to cells at 125 to 1000 nM final concentration. After 24 to 48 hours, cells were collected, washed in MACS buffer (Milteny, 130-091-221) and incubated with antibodies against the cell surface activation markers CD69-AF700 (Biolegend cat. no. 104539, clone H1.2F3, 1:100) and CD25-BV605 (Biolegend cat. no. 102036, clone PC61, 1:100) and DAPI and analyzed by FACS.

IL-10

Engineered IL-10 proteins were produced as previously described.[60] cDNA encoding human WT IL-10 or the IL-10 D25K variant was subcloned into the pD649 mammalian expression vector containing an N-terminal HA signal peptide and C-terminal 6×His tag. Vectors were transiently transfected into Expi-293F cells (Thermo, A14527) using Expifectamine transfection reagent (Thermo, A14525); 72 to 96 hours after transfection, cell supernatant was harvested and proteins were purified with Ni-NTA resin (Qiagen, 30210) followed by size-exclusion chromatography on a Superdex 200 column (GE) in PBS. Final endotoxin concentrations were determined

using a chromogenic endotoxin quantitation kit (Thermo Scientific, A39552) and were never greater than 1 endotoxin unit per mg of purified protein.

Mini-osmotic pump intracerebroventricular delivery of engineered proteins and antibodies

Purified engineered proteins or antibodies were loaded into 100 μL osmotic pumps (Alzet, 1007D) with a 7-day infusion rate of 0.5 μL per hour. Osmotic pumps were connected to a cannula (Brain infusion kit III, 0008851, Alzet) inserted using a stereotaxic frame at +1 mm lateral, -0.3 mm anterior-posterior, and -3 mm deep relative to bregma to target the right lateral ventricle. Mini-osmotic pumps deliver agents intracerebroventricularly (ICV), into the lateral brain ventricle which is directly adjacent to the SVZ and this method has been used to effectively deliver different compounds to the SVZ[28,69,70,72,73,117]. Since the ventricles are filled with cerebrospinal fluid that circulates throughout the brain, any agents delivered into the ventricles will also reach other brain regions, including the hippocampus.[85,118]

The pump was placed subcutaneously and mice received a single dose of Buprenorphine SR (0.5 mg/kg) for postoperative pain management and monitored for post-surgery until full recovery. Old male mice (24-27 months) from the NIA were used for these experiments. We also included young male mice (3 months) which were infused with vehicle control (artificial cerebral spinal fluid) in the IL-10 experiment. Surgeries were performed on heating pads with isoflurane induced anesthesia, with a Kopf (Model 940) stereotaxic frame, World Precision Instruments (UMP3T-1). Mice were weighted prior to surgery and at the end of the treatment and we never observed a significant change in the weight of the mice. For neurogenesis assays, mice were given a 1-mg dose of EdU via intraperitoneal injection two days before and on the day of mini-osmotic pump implantation.

Mouse and human (control) RIPR-PD1 proteins were loaded at 5 mg/mL (for most experiments) or 2.5 mg/mL (for the dose response experiment). To compare the efficiency of RIPR-PD1 and conventional anti-PD1 antibodies to expand T cells in the brain, we loaded anti-IgG2a isotype control (clone 2A3, BioXCell, 3mg/mL), anti-PD1 (clone RMP1-14, BioXCell, 3mg/mL) or RIPR-PD1 (3mg/mL) into mini-osmotic pumps and delivered these proteins into the lateral ventricle for a week. Our FACS analysis revealed that at the same dose RIPR-PD1 led to a significant increase in the number of T cells in the SVZ while anti-PD1 antibody did not (Figures S2A and S2B). Infusion of anti-PD1 antibodies into the brain of old mice also could result in a statistically significant increase in $CD8^+$ T cells within the aged brain (see Table S4), but the magnitude of this effect was modest, and significance was observed only with a large sample size of mice (22-23 months, n = 11-12 male mice per condition, Table S4). For this reason, we proceeded with RIPR-PD1 for the rest of our study. The stronger increase in T cell number by RIPR-PD1 is likely due to the enhanced ability of RIPR-PD1 to inhibit checkpoint blockade[68] coupled with the size of these molecules (~45kDa for RIPR-PD1 versus ~150kDa for anti-PD1 antibody), which could affect their penetration into the brain parenchyma. We did not specifically measure blood brain barrier integrity in our experiments and therefore we cannot rule out an increase in T cell infiltration upon RIPR-PD1 infusion.

Wildtype (WT) IL-10 and the engineered IL-10* variant were loaded in the mini-osmotic pumps at 0.1 mg/mL or 0.02 mg/mL. All proteins were diluted in artificial cerebrospinal fluid (CSF) (3525, Tocris). Artificial CSF was used as a vehicle control for WT IL-10 and the engineered IL-10* variant. To block type I interferons, we used anti-mouse IFNAR-1 (clone MAR1-5A3, A2121, Selleck, 1 mg/mL). Mouse anti-IgG1 (clone A2106, Selleck, 1mg/mL) was used as the isotype control. To block type II interferons, we used rat IgG1 anti-IFN-γ (clone R4-6A2, BE0054, BioXCell, 1mg/mL). Rat anti-IgG1 (clone HRPN, A2119, Selleck, 1mg/mL) was used as the isotype control. The specificity of each anti-interferon antibody for type I or type II interferons was confirmed *in vitro* using BV2 cells.

Single-cell RNA-seq of SVZ using 10x Genomics Chromium

For all single-cell RNA-seq datasets, male mice were used. SVZ neurogenic niches were collected and processed as described in ref.[8] one week after infusion with engineered proteins. Mice were sedated with 0.8 mL of 2.5% vol/vol Avertin (Sigma-Aldrich, T48402-25G) in PBS (Corning, 21-040-CV) and perfused transcardially with 15 mL of PBS with heparin sodium salt (50 U/mL, Sigma-Aldrich, H3149-50KU) to remove circulating blood cells. Brains were immediately collected into PIPES buffer (pH 7.4, Sigma-Aldrich, P1851) on ice and dissected in ice-cold PIPES buffer. The SVZ from each hemisphere was micro-dissected and dissociated with enzymatic digestion with papain (Worthington, LS003119) for 10 min at a concentration of 14 U/mL. The dissociated SVZ was triturated with a P1000 pipette in a solution containing 0.7 mg/mL ovomucoid (Sigma-Aldrich, T9253) and 0.5 mg/mL DNaseI (Sigma-Aldrich, DN25) in DMEM/F12 (Thermo Fisher, 11330032). The dissociated cells from the SVZ were then centrifuged through 22% Percoll (Sigma-Aldrich, GE17-0891-01) in PBS to remove myelin debris. After centrifugation, cells were filtered through a 35-μm snap-cap filter (Corning, 352235). At this point, cells from mice from the same condition were pooled together to avoid individual-to-individual variability: 4 old mice per condition were pooled for the RIPR-PD1 experiment in Figures 2 and 3 mice per condition were pooled for the independent experiment in Figure S3, 1 or 2 young or old mice per condition for the IL-10 experiment in Figures 3 and 3 mice per condition were pooled for the experiment in Figure S4. Pooled cells were washed once with 1.5 mL of FACS buffer B (PBS with 1% BSA (Sigma, A7979) and 0.1% glucose (Sigma-Aldrich, G7021)) and spun down for 5 min at 300*g*. Live/dead staining was performed using 1 μg/mL propidium iodide (BioLegend, 421301). For FACS gating strategy see Figure S7A. FACS sorting was performed on a BD FACS Aria II sorter, using a 100-μm nozzle at 20 psi. Live cells were sorted into 500 μl of FACS buffer B in a protein low-bind microfuge tube. Cells were then spun down at 300*g* for 5 min at 4°C and resuspended in FACS buffer B for counting and then immediately run on 10x Chromium to capture single-cell transcriptomes.

Cells were loaded onto a 10x Genomics Chromium chip per factory recommendations. Reverse transcription and library preparation was performed using the 10x Genomics Single Cell 3'v3.1kit (for the IL-10 experiments) or the 10x Genomics Single Cell 5'v2 dual

index kit (for the RIPR-PD1 experiment) following the 10x Genomics protocol. For sequencing, 8,000 cells per lane were targeted but typical yields were approximately 6,000 cells. Library were multiplexed and sequenced on the Illumina NextSeq-500 with paired-end 150 bp reads. Sequencing was done to target a minimum of 25,000 reads per cell for transcriptome characterization. Metadata for all mice used in single-cell RNA-seq experiments can be found in Table S1.

CD8$^+$ T cell isolation and analysis from the brain and lung of young and old mice

For single-cell RNA-seq on brain and lung T cells, T cells were isolated from old brains and old lungs of old mice (22-25 months, n = 11 male mice total). For validation by FACS, T cells were isolated from the brain and lung of young (6 months, n = 6 male mice per condition) and old (24 months, n = 6 male mice per condition) mice. In both types of experiments, mice were sedated with 0.8 mL of 2.5% vol/vol Avertin (Sigma-Aldrich, T48402-25G) and perfused with 15 mL of PBS with heparin sodium salt (Sigma-Aldrich, 2 mg/mL) to remove the blood. Brains were immediately collected and pushed through a 100 μm filter using the flat end of a syringe plunger. Lungs were collected after perfusion and chopped into small pieces. Tissue dissociation was carried out with 2 mg/mL collagenase type IV (Gibco, 17104019) for 60 min at 37°C in HBSS with calcium and magnesium (Gibco, 14025092), containing 14 μg/mL of DNase1 (Sigma-Aldrich). The dissociated brains and lungs were then centrifuged through 22% Percoll (GE Healthcare) in PBS to remove myelin debris. After centrifugation, cells were washed with FACS buffer B. Antibody staining was carried out in FACS buffer B at the following dilutions: CD45-PE (BioLegend 103105, Clone:30-F11, 1:100), CD8-FITC (BioLegend 100705, Clone:53-6.7 1:100), CD8a-BV785 (BioLegend 100749, Clone: 53-6.7, 1:200), CD11b-PerCP/Cy5.5 (BioLegend 101227, Clone:M1/70, 1:100), CD3-AF700 (BioLegend 100216, Clone:17A2, 1:100), CD25-PCP (BioLegend 102027, Clone: PC61, 1:200), PDI-FITC (BioLegend 135213, Clone: 29F.1A12, 1:200), LAG3-BV711 (BioLegend 125243, Clone: C9B7W, 1:200), CD44-BV605 (BioLegend 103047, Clone: IM7, 1:200), CD69-BUV661 (BD 741478, Clone: H1.2F3, 1:200), and CD4-BUV496 (BD 612952, Clone: GK1.5, 1:200). Viability staining was performed with 1 μg/mL DAPI (Thermo Fisher, 62248) or Fixable Near-IR Dead Cell Stain Kit (Thermo Fisher, L10119). For analysis, samples were acquired on a Symphony flow cytometer (BD) and analyzed with FlowJo software (Tree Star), and CD8$^+$ T cells were defined as CD45$^+$CD11b$^-$CD3$^+$CD8$^+$. FACS sorting was performed on a BD FACS Aria II sorter, using a 100-μm nozzle. Cells were sorted into FACS buffer B. CD8$^+$ T cells were defined as CD45$^+$CD11b$^-$CD3$^+$CD8$^+$. For FACS gating strategy see Figure S7B. In total, 10,000 cells were sorted from each lung and pooled together. The entire sample was sorted for all 11 brains, obtaining between 800-4,000 cells per brain and all cells were pooled together. Cells were then spun down at 300*g* for 5 min at 4°C and resuspended in FACS buffer B for counting and then immediately run on 10x Chromium to capture single-cell transcriptomes.

Cells were loaded onto a 10x Genomics Chromium chip per factory recommendations. Reverse transcription and library preparation was performed using the 10x Genomics Single Cell 5'v2 dual index kit following the 10x Genomics protocol to obtain both whole single-cell transcriptomes and T cell receptor sequences. For sequencing, 8,000 cells per lane were targeted but typical yields were approximately 4,000 cells. Library were multiplexed and sequenced on the Illumina NextSeq-500 with a high output (400m) kit. Sequencing was done to target a minimum of 25,000 reads per cell for transcriptome characterization. Even though we sorted CD8$^+$ T cells by FACS for this experiment, initial clustering of cells showed small populations of other cell types including alveolar macrophages, B-cells, monocytes, neutrophils and microglia. These cell types were filtered out and subsequent analysis was performed only on the remaining T cells.

Quality control of 10x Genomics single-cell RNA-seq

Cell Ranger (version 3.0.2) default settings were used to distinguish cells from background. Subsequent analysis was performed using R (version 4.2.2). Cells were filtered out in Seurat (version 4.3.0) if they contained fewer than 500 genes or greater than 10% mitochondrial reads. Small clusters of doublets that shared several marker genes from pure populations were identified and removed.

Seurat was used for SCT normalization, dimensionality reduction, clustering, and marker gene identification. Cell types in all datasets were manually annotated as described in ref.[8]. Major cell clusters were identified in Seurat using FindClusters(), and marker genes were identified using FindAllMarkers(). Cell types were determined using marker genes identified from the literature and the marker genes were cross-referenced with annotations present in the single-cell database PanglaoDB. This analysis identified ~11 clusters of cells (depending on the dataset), including astrocytes and qNSCs, aNSCs and NPCs, neuroblasts, neurons, oligodendrocyte progenitor cells, oligodendrocytes, endothelial cells, 'mural' cells (pericytes or smooth muscle), ependymal cells, macrophages, T cells and microglia. The genes used for identification are included in Table S1 and a clustering of a subset of these genes is presented in Figures S3A and S4B. Consistent with our previous studies,[8,50,58,75] we did not observe sufficient differences in transcriptomic signatures to separate astrocytes from qNSCs and aNSCs from NPCs. We have described these clusters as 'astrocyte/qNSCs' and 'aNSC/NPCs' throughout the present study. Consistent with our previous studies, we also identified only a few ependymal cells in several of our datasets, although these cells are known to be numerous in the SVZ neurogenic niche. This is probably because ependymal cells are too big to be efficiently uploaded in droplets and/or they are sheared in the 10x microfluidic device.

Clustering, heatmaps, and violin plots for gene expression in single cells

Hierarchical clustering and heatmap generation were performed for single cells on the basis of log-normalized (with scale factor 10,000 and pseudocount 1) expression values of marker genes curated from literature or identified as highly differentially expressed. Heatmaps were generated using the heatmap.2 function from the gplots (version 3.1.3) R package using the default complete-linkage

clustering algorithm. To visualize the expression of individual genes, cells were grouped by their cell type as determined by analysis with Seurat. Log-normalized gene expression values were plotted for each cell as a violin plot with an overlying dot plot in R.

Calculation of immune cell proportions and differentially expressed genes

Processed single-cell datasets[8,50] were merged using Seurat (version 4.3.0.1). The two datasets were integrated with Harmony (version 1.2.0[119]). Differential gene expression between young and old samples was calculated using the 'FindMarkers' function in Seurat (with the MAST algorithm) in individual cell-types. Benjamini-Hochberg FDR was applied, and significant differentially expressed genes were defined at FDR < 0.05. For each cell-type the total proportion of cells within the young/old datasets was calculated as a log2(fold-change) value compared to the total number of cells in the sample and visualized along with cell-type DEG data using ggplot2 (version3.4.3).

T cell state scoring in single-cell RNA-seq data

Mouse T-cell signatures were constructed using the SignatuR library (version 0.1.2) and leveraged with the UCell package (version 2.4.0[120]) to calculate a score for each T cell with the 'AddModuleScore_UCell' function.

Signatures were defined as follows:

- T cell terminal exhaustion: *Gzmk, Pdcd1, Tigit, Lag3, Havcr2, Ctla4, Tox, Eomes, Cd244/2B4, Nr4a1, Nr4a2, Nr4a3, Batf, Irf4, Cd160, Cd101, Entpd1, Prdm1*
- T cell stemness/memory: *Tcf7, S1pr1, Lef1, Ccr7, Sell, Il7r, Cd62l*
- T cell cytotoxicity/effector: *Gzma, Gzmb, Prf1, Faslg, Tnf, Il2, Ifng, Cd69*

The ggpubr library version 0.6.0 was used to generate boxplots. For the IL-10 experiment, we used a label-swapping approach to calculate an empirical *P*-values, since there were only 9 T cells in the old control sample. We estimated the likelihood of observing the absolute difference in average signature score between treatment and control T cells (and between WT-IL10 and IL10* treatments) by randomly swapping labels of control/treated cells and re-calculating signature differences. This label swapping was done 10,000 times to ensure stability of our estimates and reported as the probability of obtaining the observed signature difference by chance.

Inflammation score

The set of genes that were differentially expressed in microglia upon WT IL-10 and IL-10* treatment was compared to the direction-of-effect of these genes in microglia from young and old SVZ samples (taken from refs.[8,50] datasets). We then defined custom signatures for pro- and anti-inflammatory effects with the 'SignatuR' library (version 0.1.2). Genes increasing in expression in microglia from old SVZs were aggregated into a pro-inflammatory signature (*H2-Aa, H2-Ab1, H2-DMa, H2-Oa, H2-Ob, Stat1, Bst2, Isg15, Ifit1, Ifit2, Ifit3, Ifitm3, Ifi27, Ifi27l2a, B2m, H2-K1, H2-D1, Ccl4, Ccl3, Ccl5*), while genes decreasing in expression in old SVZ microglia were aggregated into an anti-inflammatory signature (*Il10ra, Il10rb, Jak1, Tyk2, Stat3, Socs3, Hmox1, Blvra, Etv3, Cdkn2d*). Additionally, given that part of IL10's effects are mediated through repression of inflammatory signaling, we included the following genes in the anti-inflammatory signature – but negated their effects in the SignatuR signature such that decreased-expression contributes to a stronger signature score: *Il1a, Il1b, Il6, Tnf, Nfkbia*. These signatures were then used to calculate UCell scores with the UCell package (version 2.4.0) for all cells of a given cell-type in our datasets, after separating cells into treated and control groups. For a given comparison and cell-type (e.g. WT IL-10 compared to control for microglial cells), we took the average UCell score for treated cells and divided by the average UCell score for untreated (control) cells. Taking the log2 of this ratio, we calculated the fold-change in signature activity for a given treatment. This was calculated across all treatments and conditions and plotted using ggplot2 version 3.4.3.

Single-cell RNA-seq differential expression and pathway enrichment analysis

MAST (implemented in FindMarkers() in Seurat) was used for differential gene expression analysis for each cell type. In each experiments cells from the treatment condition were compared to their control sample. For microglia pathway enrichment, the top 100 genes significantly (adjusted *P*-value <0.05) up or downregulated in microglia were imputed into EnrichR.

For GSEA analysis to identify pathways that change with RIPR-PD1, WT IL-10 or IL-10*, the differential-expression gene list from MAST was ranked by decreasing Log2Fold Change, then pathway enrichment was performed using the gseGO function from the clusterProfiler package (version 4.8.3), based on the GO biological processes dataset included in the org.Mm.eg.db package (version 3.17.0). Resulting enrichments were collapsed for semantic similarity using the 'simplify' function from clusterProfiler and visualized with ggplot2.

Effect of immune interventions on aging clocks and clock genes

To measure the effect of different interventions on the transcriptomic aging clocks, we examined the distribution of predicted ages by cell-type-specific aging clocks as described in ref.[58]. We ploted the predicted age scores in violin plots and density plots using ggplot. We calculated the effect by the difference in median predicted age between intervention and control. In dot plots, these differences were represented as 'effect', using size and intensity of color, with blue indicating 'rejuvenation' (younger than actual age) and red indicating 'aging' (older than actual age).

PCA analysis of the neurogenic niche

Control samples (young and old mice treated with artificial cerebrospinal fluid from the IL-10 experiment) were used to establish the effects of aging across the entire subventricular zone using principal-components analysis. First, genes significantly changing with age across the niche were identified using a mixed-effects model implemented in MAST via the 'FindMarkers' function from Seurat, with the following parameters: test.use = "MAST", mic.pct=0.10, logfc.threshold = log(1.1), random.seed = 3, max.cells.per.ident = 1000). *P*-value adjustment was subsequently performed using the Benjamini-Hochberg method, with significance defined as FDR < 0.05. The Seurat object was subset to these significant age-DEGs and normalized using the SCTransform method. Next, we determined the number of calculated PCs which best captured the differentiation between the young and old neurogenic niche. For a given number of PCs, we performed PCA using the prcomp_irlba function from the irlba library version 2.3.5.1. We then calculated the collective distance between young and old cells in this PCA space, incorporating all PCs, using the Mahalanobis distance function in R. We aggregated these collections of PCs to better interpret differences between young and old cells. Thus, for each PC, we calculated the value of all young and old cells, and subsequently compared the distribution of values using the Student's t-test. Only those PCs for which significant (differences between young/old cells were observed were retained (Student's t-test p-value < 0.05). Retained PCs were grouped based on the direction-of-effect with respect to age (positive and negative). We then aggregated these PCs by weighing each by the significance (-log10 p-value) of the young/old t-test. We then similarly calculated the distances between young/old cells using the weighted sums of these aggregated PCs. To identify the ideal number of PCs to use, we iterated through 10-100 PCs, calculating the aggregate Mahalanobis distance between young/old cells at each iteration. We selected n = 98 as the number which yielded the largest average distance between young and old cells. Next, we took this reference PCA space – along with the aggregated PCs, and considered our different treatment datasets. For each dataset, we subset the expression matrix to match the set of genes used in the initial reference definition, normalized with SCTransform, and subsequently projected the expression data into this reference PCA space. We then calculated the position of treated cells along our two aggregated PC vectors, allowing us to calculate the relative Mahalonobis distance of cells to the centroids of the young and old clusters. We converted these distances to a single metric: (Distance to young centroid) – (Distance to old centroid), such that negative values indicate greater proximity to the younger-cell distribution, and vice-versa. Finally, we visualized the distribution of this distance metric across all cells in each treatment using the 'geom_density_ridges' function from the ggridges package version 0.5.4.

MERFISH spatial transcriptomic analysis of T cells in the mouse brain

MERFISH data analysis was performed on a previously published dataset of brain aging in male mice.[7] For this analysis, we removed putative doublets using Scrublet[121] and a doublet score cutoff of 0.18. We then filtered out all cells with segmentation volume less than 100 or greater than three times the median cell volume. We also filtered out all cells with less than 20 counts and/or less than 5 genes with non-zero expression. To correct for different segmentation sizes, we divided the raw transcript counts obtained for each cell in the MERFISH dataset by the volume of the corresponding segmentation. We then filtered out all cells in the top 2% highest and top 2% lowest total expression. Log-normalization was performed by normalizing the total gene expression per cell to 250 and then performing a natural log transform of the normalized values.

We identified cell type clusters by log-normalizing the counts in the MERFISH data and then computed z-scores with maximum value 10. We performed Leiden clustering and labeled each cluster based on cell type expression patterns in the UMAP visualization and in the heatmaps of cell type markers. For clusters that expressed markers from multiple cell types, we performed successive Leiden clustering on those clusters until distinct cell types could be annotated. We identified cell clusters for T cells and other cell types (astrocytes, microglia, oligodendrocytes, endothelial cells, mural cells, macrophages). To quantify the expression of exhaustion/effector/memory markers in the T cell cluster, we use signature scores, which are computed as the sum of log-normalized gene expression for the genes in each score (see gene lists below). We performed the same analysis to quantify gene signature scores in microglia. Statistical significance was calculated with two-sided Mann-Whitney U-tests.

Gene signatures:

- Exhausted T cells: *Gzmk, Pdcd1, Tigit, Lag3, Ctla4, Tox, Nr4a2*
- Effector T cells: *Gzmb, Tnf, Ifng, Cd69*
- Memory T cells: *Tcf7, Ccr7, Sell, Il7r*
- IL-10 signature in microglia: *Il10ra, Il10rb, Il10, Jak1, Socs3, Stat3, Tgfb1*

Pro-inflammatory signature in microglia: B2m, H2-D1, H2-K1, Ifit1, Ifi27, Bst2, Ifitm1, Ifitm3, Ccl5, Ccl4, Stat1

Microglia FACS *in vivo*

The SVZ was isolated and dissociated into a single cell suspension as described above for 'Single-cell RNA-seq using the 10x Genomics Chromium single-cell technology'. We used T cells from the spleen or OneComp eBeads (eBioscience, 01-1111-42) to perform single-stain FACS controls for compensation and gating. For this, we removed the spleen and placed it on a 70 μm cell strainer on top of a 50 mL conical tube. We used the flat end of a syringe plunger to mince the spleen by crushing the spleen 5 times in gentle circular motions. FACS buffer B was added to wash the cell strainer and the sample was centrifuged (3 min, 1200rpm, 4°C). ACK lysing buffer (Thermo Fisher, A1049201) was added to lyse red blood cells. After the lysis of red blood cells, 10 mL of FACS buffer

B was added and samples were spun for 3 min, 1200rpm at 4°C. After centrifugation cells were resuspended in FACS buffer B and filtered through a 40 μm cell strainer to remove clumps and were then ready for staining with antibodies.

Antibody staining was carried out in FACS buffer B at the following dilutions: CD45-PE (BioLegend cat. no. 103105, Clone:30-F11, 1:100), CD11b-PerCP/Cy5.5 (BioLegend cat. no.101227, Clone:M1/70, 1:100), CD8-APC (BioLegend cat. no. 100705, Clone:53-6.7, 1:100), BST2-FITC (BioLegend, cat. no.127007, Clone:927, 1:100), H-2Kb/Db-PE-Cy7 (BioLegend, cat. no. 114717, Clone:34-1-2S, 1:200), CD86/B7-2-FITC (Biolegend, cat. no. 105005, Clone: GL-1, 1:100) and TruStain FcX (Biolegend, cat. no. 101319, Clone: 93, 1:100) for 30-60 minutes at 4°C. Samples were washed with 1 mL of FACS buffer B and resuspended in FACS buffer B containing 1 μg/mL DAPI (Thermo Fisher, 62248). Fluorescent-minus-one controls were used to set positive gates in each experiment. Microglia were defined as $CD45^+$, $CD11b^+$, $CD8^-$. For FACS gating strategy see Figure S7C. Samples were analyzed on a BD LSRII. Compensation was performed with OneComp eBeads or splenocytes stained with single antibodies or DAPI. All FACS data analysis was performed in FlowJo.

T cell FACS *in vivo*

The SVZ was isolated and dissociated into a single cell suspension as described above for 'Single-cell RNA-seq using the 10x Genomics Chromium single-cell technology'. Antibody staining was carried out in FACS buffer B at the following dilutions: CD45-PE (BioLegend cat. no. 103105, Clone:30-F11, 1:100), CD11b-PerCP/Cy5.5 (BioLegend cat. no.101227, Clone:M1/70, 1:100), CD8-FITC (BioLegend, cat. no. 100705 Clone:53-6.7, 1:100), CD4-APC (BioLegend, cat. no. 100411 Clone: GK1.5, 1:100), CD3-AF700 (BioLegend, cat. no.100216 Clone: 17A2, 1:100), for 30-60 minutes at 4°C. Samples were washed with 1 mL of FACS buffer B and resuspended in FACS buffer B containing 1 μg/mL DAPI (Thermo Fisher, 62248). Fluorescent-minus-one controls were used to set positive gates in each experiment. $CD8^+$ T cells were defined as $CD45^+CD11b^-CD3^+CD8^+CD4^-$. Samples were analyzed on a BD LSRII. Compensation was performed with splenocytes stained with single antibodies or DAPI. All FACS data analysis was performed in FlowJo.

Immunostaining of brain sections

Mice were subjected to intracardiac perfusion with 10 mL of PBS containing heparin followed by 15 mL of 4% paraformaldehyde in PBS. Brains were post-fixed for 24 h in 4% paraformaldehyde (Electron Microscopy Sciences, 15714). They were then subjected to dehydration in 30% sucrose Sigma-Aldrich, S3929). Brains were subsequently embedded in optimal cutting temperature compound (OCT, Tissue-Tek/Electron Microscopy Services 62550-12) in cryomolds and frozen in a dry ice/ethanol bath. Brains were sectioned into 14 μm coronal sections with a cryostat (Leica, CM3050S) and mounted on electrostatic glass slides (Fisher Scientific, 12-550-15). For SVZ imaging, we began taking slices at the most anterior part of the lateral ventricle, collecting SVZ sections every 168 μm onto the slide.

To perform immunofluorescence staining, sections were first washed with PBS, followed by permeabilization in ice-cold methanol with 0.2% Triton-X (Fisher Scientific, BP151) for 10 min at room temperature. Antigen retrieval was performed in 10 mM sodium citrate buffer (pH 6.0; 2.94 g Tri-sodium citrate dihydrate (Sigma-Aldrich, S1804) in 1,000 mL milliQ H_2O adjusted to pH 6.0 with 1 N HCl) + 0.05% TWEEN 20 (Sigma-Aldrich, P1379-1L) in a 85°C water bath for 2 h. Slides were then cooled to room temperature for 20 min and washed 3 times with PBS. Sections were blocked with 5% normal donkey serum (ImmunoReagents, SP-072-VX10) and 1% BSA (Sigma, A7979) in PBS for 30 min at room temperature. Primary antibody staining was performed overnight at 4°C in 5% normal donkey serum and 1% BSA in PBS. Primary antibodies used were the following: CD3 (Novus Biological, NB600-1441, Clone: SP7, lot: L139 and J275, 1:200), CD68/ macrosialin (Biolegend, 137001, Clone: FA-11, lot: B290801, 1:500), CD8α (BioLegend, MCA609, clone:KT15, 1:200), DCX (Cell Signaling Technology, 4604S, 1:500), GFAP (Abcam, ab53554; 1:500), IBA1 (Novus Biological, NB100-1028, lot: S7C7G2P24-E250517, 1:500), IFITM3 (Abcam, ab15592, 1:500), Ki67 (eBioscience, Clone: SolA15, lot: 4328926, 1:500), NeuN (EMD Millipore, MAB377, Clone: A60, lot: 2919676, 1:500), P2RY12 (gift from Michelle Monje, 1:1000), OLIG2 (R&D Systems, AF2418, lot: UPA0821081, 1:100), PD1 (R&D Systems, AF1021, lot: GQA0423071, 1:150), STAT1 (Cell Signaling, 14994, Clone: D1K9Y, lot: 4, 1:500), TMEM119 (Synaptic Systems, 400004, 1:500). We also tried antibodies against phospho-STAT1 (pY701, clone 4a, BD), total STAT3 (D3Z2G, CST 12640), phospho-STAT3 (Ser727, CST 9134) and SOCS3 (Abcam Ab16030, Novus biologicals NBP2-27116, CST 52113) but could not obtain reliable staining with these antibodies with or without antigen retrieval. Sections were washed with PBS with 0.2% TWEEN 20 and then with PBS only 3 times each for 5 min at room temperature. Secondary antibody staining was performed at room temperature for 2 h in 5% normal donkey serum and 1% BSA in PBS. Secondary antibodies used were the following: donkey anti rabbit-AF568 (Thermo Fisher, 1:500), donkey anti rat-AF488 (Thermo Fisher, 1:500) and donkey anti goat-AF647 (Thermo Fisher, 1:500). Sections were washed with 0.2% TWEEN 20 and then with PBS 3 times each for 5 min at room temperature. Sections were stained with DAPI at 1 μg/mL (Thermo Fisher, 62248) for 10 min at room temperature. Sections were mounted with ProLong Gold Antifade Mountant with DAPI (Thermo Fisher, P36931. Images were acquired on a Zeiss LSM 900 confocal microscope and ZEN Blue 3.0 software or a Nikon Eclipse Ti microscope equipped with a Zyla sCMOS camera (Andor) and NIS-Elements software (AR 4.30.02, 64-bit) using the 20× or 60× objective. Image acquisition was blinded. For visualization of images displayed in this manuscript, brightness and contrast were adjusted in Fiji to enhance visualization (these adjustments were not performed before the quantification described below). The same settings were applied to all images shown for each experiment.

We stained brain sections containing the SVZ from young and old mice with antibodies against IBA1, TMEM119 and P2RY12, all markers of microglia/myeloid cells. We found that there was great overlap between these markers in both young and old mice

indicating that most myeloid cells in the brain are indeed microglia. For our experiments, we used IBA and TMEM119 antibodies due to antibody species compatibility.

Confocal microscopy image analysis and quantification

T cell quantification

$CD8^+$, $CD8^+Ki67^-$, $CD8^+Ki67^+$, $CD8^+PD1^+$, $CD8^+PD1^-$, $CD8^+Ki67^+PD1^+$, or $CD8^+Ki67^+PD1^-$ T cells were manually counted in the SVZ region. For young and old mice 2-3 coronal sections were quantified. For RIPR-PD1 3 coronal sections were quantified for each mouse and averaged. *P*-values were calculated using the Wilcoxon rank-sum test.

STAT1 and IFITM3 quantification

The entire SVZ area in both brain hemispheres was imaged using the 20× objective in 2-6 coronal brain sections per mouse. Fiji (ImageJ) was used for image analysis. The STAT1 or IFITM3 fluorescence co-localizing with the microglia cell markers IBA1 or TMEM119, the oligodendrocyte marker OLIG2 or the astrocyte/NSC markers GFAP or SOX2 was quantified using a custom pipeline. The cell type marker channel was used to generate a mask by setting intensity thresholds to outline the positive areas. The same threshold values were used for all images across all conditions in each individual experiment. The cell masks were then used to determine STAT1 or ITIM3 fluorescence by mean intensity per masked pixel. The mean intensity STAT1 or IFITM3 values for each image were normalized by the number of $DAPI^+$ nuclei to account for differences in the number of cells. To combine data from different experiments, we normalized each independent experiment by dividing by the median intensity of the control samples and the mean of these normalized values was used for plotting and calculating *P*-values using the Wilcoxon rank-sum test.

CD68 in IBA1 cells quantification

The entire SVZ area in both brain hemispheres was imaged using the 20× objective in 2-6 coronal brain sections per mouse. For the hippocampus the entire DG region was imaged in one hemisphere in 4 sections per mouse. Fiji (ImageJ) was used for image analysis. The CD68 fluorescence co-localizing with the microglia cell marker IBA1 was quantified using a custom pipeline. The IBA1 channel was used to generate a mask by setting intensity thresholds to outline the positive areas. The same threshold values were used for all images across all conditions in each individual experiment. The cell masks were then used to determine the CD68 fluorescence by mean intensity per masked pixel. *P*-values were calculated using the Wilcoxon rank-sum test.

DCX in the SVZ quantification

The entire SVZ area in both brain hemispheres was imaged using the 20x objective. Three brain sections were imaged per mouse. Cell counting was performed QuPath 0.2.3. Nuclei were segmented based on DAPI staining, and then nuclear masks were expanded by 2 μm to define the cytoplasm. Cells were identified as DCX^+ based on a threshold for mean cytoplasmic DCX intensity. For quantification of DCX intensity, Fiji (ImageJ) was used to measure average DCX signal above background for each image.

DCX, NeuN, and EdU quantification in the olfactory bulb

The entire olfactory bulb in both brain hemispheres was imaged using 20x objective and tile scanning. Images were collected from young control (4 months, n = 5 male mice), old control (24-27 months, n = 9 male mice), old WT IL-10 (0.1 mg/mL, 24-27 months, n = 10 male mice), and old IL-10* (0.1 mg/mL, 24-27 months, n = 8 male mice) mice from two cohorts, and from old control (5 mg/mL, 24-26 months, n = 6 male mice) and old RIPR-PD1 (5 mg/mL, 24-26 months, n = 6 male mice) infused mice. Six brain sections were imaged per mouse. Fiji (ImageJ) was used to calculate the area encapsulating the granule layer, inner plexiform layer, and mitral layer was for each olfactory bulb. The number of DCX^+EdU^+ and $NeuN^+EdU^+$ cells were manually counted. The mean number of DCX^+EdU^+ and $NeuN^+EdU^+$ per mm^2 was obtained from the six sections and used for plotting and calculating *P*-values using the Wilcoxon rank-sum test.

Measuring IL-6 and TNFα production in stimulated primary microglia and BV2 microglia cells with ELISA

BV2 microglia cells were seeded onto poly-D-lysine (PDL, 0.05 mg/mL in PBS; Sigma-Aldrich P6407) coated 24-well plates (75,000 cells/well) and stimulated with Lipopolysaccharides (LPS) from Escherichia coli O111:B4 (5 μg/mL, Sigma-Aldrich, L2630) alone or in combination with increasing concentrations of WT IL-10 or IL-10* for 48 hours. We used 3 different concentrations of WT IL-10 and IL-10*: 10 nM, 1 nM and 0.1 nM and found that they all suppressed the production of IL-6 and TNFα induced by LPS to a similar extent. Primary microglia were stimulated with LPS (0.1 μg/mL, we found that 5 μg/mL caused excessive stimulation) alone or in combination with increasing concentrations of WT IL-10 or IL-10* for 48 hours. We found similar results with 10nM and 1nM IL-10. Supernatant was collected and IL-6 (ELISA MAX™ Deluxe Set Mouse IL-6, Biolegend, 431304) and TNFα (ELISA MAX™ Deluxe Set Mouse TNFα, Biolegend, 430904) proteins were measured by ELISA as per the manufacturer's instructions.

IL-10 signaling assays in mouse primary T cells and BV2 microglia cells

IL-10 signaling assays were performed as previously described.[60] BV2 microglia cells or mouse primary T cells were plated in 96-well plates and stimulated with WT IL-10 or engineered IL-10* for 25 min at 37°C, followed by fixation with 1.6% paraformaldehyde (Electron Microscopy Sciences) for 10 min at room temperature. The cells were immediately permeabilized for intracellular staining by treatment with ice-cold methanol (Fisher) for 20 min at 4°C. IL-10 signaling in cells was then assessed by intracellular FACS. Permeabilized cells were incubated with Alexa Fluor 647–conjugated Anti-Stat3 (pY705) antibody (1:50, BD, clone 4/P-STAT3) for 1 hour at room temperature in intracellular FACS buffer A (PBS pH 7.2 Ca/Mg-free (Corning, 21-040-CV) with 1% FBS and 2mM EDTA (Promega, PR-V4231). The background fluorescence of the unstimulated samples was subtracted from all samples. Data were acquired using a LSRII flow cytometer (Beckman Coulter). The mean fluorescence intensity (MFI) values were background-subtracted and

normalized to the maximal wild-type IL-10 value (maximal wild-type signal set to 100%) within each experiment and plotted in Prism 8 (GraphPad). The dose-response curves were generated using the ''sigmoidal dose-response'' analysis in Prism.

Co-culture of primary T cells and primary microglia or BV2 microglia cells to measure interferon and IL-10 signaling

To set up the BV2 co-cultures, 24-well plates were coated with Poly-D-Lysine (Sigma-Aldrich P6407, 50 μg/mL) for 1 hour at 37°C and washed with PBS. BV2 microglia cells (50,000 cells) and primary T cells (20,000 cells) were added to each well after being resuspended in T cell media. For primary microglia, the cells were already attached to 6 well plates and 50,000 T cells were added per well. WT IL-10 or IL-10* was added to indicated wells at a final concentration of 10 nM. Indicated wells also received anti-interferon-γ (Bio X Cell cat. no. BE0054, Clone: R4-6A2, 0.1 mg/mL) or an IgG1 isotype control (Bio X Cell cat. no. BE0290, Clone: TNP6A7, 0.1 mg/mL). To sediment T cells onto BV2 microglia cells, plates were spun at 300g for 5 minutes. Primary microglia or BV2 microglia cells and T cells co-cultures were incubated at 37°C for 72 hours.

For FACS analysis, the co-culture media containing T cells was collected, T cells were pelleted by centrifugation, and a fraction of the supernatant was collected and immediately frozen for future analysis by ELISA. Primary microglia were washed with PBS, lifted off each well with trypsin-EDTA and combined with T cells. Cells were washed with FACS buffer A and incubated with a viability dye (APC-Cy7, Biolegend, 423105) in PBS. Cells were washed in FACS buffer A and incubated with anti-BST2-PE (Biolegend, Clone: 927, 1:200), anti-CD11b-PerCP/Cy5.5 (Biolegend, clone M1/70, 1:400), anti-CD45-PacBlue (Biolegend, 1:400), anti-CD8a-BV785 (Biolegend, Clone: 53-6.7, 1:200), anti- H-2Kb/H-2Db-FITC (Biolegend, clone 28-8-6, 1:400), and TruStain FcX (Biolegend, Clone: 93, 1:100) in FACS buffer A for 30 minutes on ice protected from light. After antibody incubation, cells were washed with FACS buffer A. Samples were analyzed on BD LSRII, gating for live cells (Live/dead-), primary microglia ($CD45^+$, $CD11b^+$, $CD8a^-$, $DAPI^-$), and T cells ($CD45^+$, $CD11b^-$, $CD8a^+$, $DAPI^-$). For FACS gating strategy see Figure S7D. 50,000 events were recorded per condition. FACS data analysis was performed in FlowJo.

For FACS analysis, BV2 microglia cells and T cells wells were washed with PBS and cells were lifted off each well with TrypLE Express (Gibco 12604013). Cells were washed with FACS buffer A twice and incubated with anti-BST2-FITC (Biolegend, cat. no. 127008, Clone: 927, 1:100), anti-CD8a-APC (Biolegend, cat. no. 100712, Clone: 53-6.7, 1:100), and TruStain FcX (Biolegend, cat. no. 101319, Clone: 93, 1:100) in FACS buffer A for 30 minutes on ice protected from light. After antibody incubation, cells were washed twice with FACS buffer A and resuspended in FACS buffer A with 1 μg/mL DAPI (Fisher Scientific 62248). Samples were analyzed on BD LSRII, gating for live cells ($DAPI^-$), BV2 microglia cells ($CD8a^-$, $DAPI^-$), and T cells ($CD8a^+$, $DAPI^-$). For FACS gating strategy see Figure S7E. 20,000 events were recorded per condition. FACS data analysis was performed in FlowJo.

To perform an IL-10 signaling assay on co-cultures of primary T cells and BV2 microglia cells, T cells were isolated from the spleen and lymph nodes (see above for isolation). After T cells were rested for 24 hours, T cells were incubated with anti-CD8a-FITC (Biolegend, cat. no. 5H10-1, 1:100) and TruStain FcX (Biolegend, cat. no. 101319, Clone: 93, 1:100) in FACS buffer A for 30 minutes on ice protected from light. BV2 microglia cells (200,000 cells per well) and T cells (80,000 cells per well) were added to a 96-well plate and stimulated with WT IL-10 (10 nM) or IL-10* (10 nM) for 30 minutes at 37°C. Following treatment, cells were fixed with 1.6% paraformaldehyde (Electron Microscopy Sciences) for 10 min at room temperature on a shaker at 500rpm. The cells were permeabilized for intracellular staining by treatment with ice-cold methanol (Sigma-Aldrich, 34860) for 20 min at 4°C on a shaker at 500rpm. The cells were washed once in intracellular FACS buffer A and then incubated with Alexa Fluor 647–conjugated anti-Stat3 (pY705) antibody (1:100, BD, clone 4/P-STAT3) in FACS buffer A for 1 hour at room temperature protected from light on a shaker at 500rpm. Cells were washed in FACS buffer A twice and analyzed on a BD LSRII. FACS data analysis was performed in FlowJo.

Measuring IFN-γ and granzyme B production in primary T cells with ELISA

Conditioned media was collected from T cells cultured with WT IL-10 or IL-10* alone or together with primary microglia for 72h and immediately frozen. IFN-γ (ELISA MAX™ Deluxe Set Mouse, Biolegend, 439404), IFN-α (ELISA MAX™ Deluxe Set Mouse IFN-α1, Biolegend, 447904), IFN-β (ELISA MAX™ Deluxe Set Mouse IFN-β, Biolegend, 439404) and granzyme B (Mouse Granzyme B DuoSet ELISA, R&D Systems, DY1865-05) proteins were measured by ELISA as per the manufacturer's instructions. IFN-α and IFN-β were not detected in the conditioned media.

Nest-building behavior assay

The nesting assay was completed to assess well-being adapting protocols described previously.[122] Mice were provided with unstructured nesting material (~10 grams of Enviro-dri ® natural brown material, Shepherd Specialty Papers) 2 hours after surgery to implant mini-osmotic pumps. Mice were given 48 hours to build nests in their home cages. After 48 hours, pictures of the nests were taken with an iPhone camera, and a blinded experimenter scored these pictures with a score (1-4) based on the quality of nests. A score of 1 = no nest built and a score of 4 = an enclosed nest. *P* values were calculated using the Wilcoxon rank-sum test.

Cognitive testing in old mice

Mini-osmotic pumps containing control vehicle or engineered IL-10* (0.02 mg/mL) were implanted into the lateral ventricle of old male mice (21 months, n = 15 male mice). Mice were randomly assigned to each treatment group. Health was regularly assessed, and mice were weighed during the course of treatments and testing. The numbers of mice used to result in statistically significant differences were calculated using standard power calculations with a = 0.05 and a power of 0.8. We used an online tool to calculate power (https://www.stat.uiowa.edu/~rlenth/Power/index.html) and sample size based on experience with the respective tests, variability

of the assays and inter-individual differences within groups. Two weeks post-surgery behavioral testing was performed (the agents were infused for a week, and we allowed another week for the mice to recover). Three days before testing, mice were habituated to the investigator for 1 minute per day. Following this habituation, mice were tested in the forced alternation Y maze followed by the novel object recognition test. Two mice from the control group died before testing.

Forced alternation Y maze test

The Y Maze task was conducted as previously described.[87] During the training phase, the mice were placed into the start arm facing the wall and were allowed to explore the start and trained arm for 5 min, while the entry to the 3rd arm (novel arm) was blocked by an opaque door. The maze was cleaned between each mouse to remove odor cues, and the trained arm was alternated between mice, for half of the mice the right arm of the maze was blocked during training while for the other half the left arm was blocked. After training, the mouse was returned to its home cage. After 45 min, the mouse was returned to the start arm and was allowed to explore all three arms for 5 min. The number of entries in each arm was quantified using the Smart Video Tracking Software (Panlab; Harvard Apparatus) and *P* values were calculated with a two-way ANOVA test, using Sidák's post-hoc test. The percentage of entries in each arm was defined as the number of entries in each arm divided by the total number of entries in all arms during the first minute of the task. The discrimination index was quantified by (novel arm − trained arm)/(novel arm + trained arm). *P* values were calculated with a two-tailed one-sample *t*-test to compare the discrimination index for each group to chance (zero). To compare between groups *p* values were calculated with a two-sided Wilcoxon rank sum test (all statistics are reported in Table S4). Mice that did not perform three entries during the first minute of testing were excluded. This included 2 mice from the control group (in addition to the 2 mice that died) and 1 from the IL-10* group, resulting in a final 11 mice for control and 14 mice for IL-10* for this test (Table S4).

Novel object recognition test

The NOR task was performed as previously described.[87] On day one (the habituation phase), mice performed open field testing by exploring an empty arena for 10 min. Infrared photobeam breaks were recorded and movement metrics were analyzed using the MotorMonitor software (Kinder Scientific). On day two (the training phase), two identical objects were placed at equal distances from two of the corners into the habituated arena, and the mice (placed facing the wall on the opposite side of the box from the objects) were allowed to explore for 5 min. On day three (the testing phase), one object was replaced with a novel object, and the mice were allowed to explore for 5 min. The time spent exploring each object was quantified using the Smart Video Tracking Software (Panlab; Harvard Apparatus). Two different sets of objects (a custom Lego figurine and a glass vial with green tape filled with water, both ~12 cm in height) were used. To control for any inherent object preference, half of the mice were exposed to object A as their novel object and half to object B. To control for any potential object-independent location preference, the location of the novel object relative to the trained object was also counterbalanced for each mouse. To determine the percentage of time with the novel object, we calculated (time with novel object)/(time with trained object + time with novel object) × 100. *P* values were calculated with a two-tailed one-sample *t*-test to compare the discrimination index for each group to chance (50%). To compare between groups, *P* values were calculated with a two-sided Wilcoxon rank sum test (all statistics are reported in Table S4). Mice that did not explore both objects during the training or testing phase were excluded from the analysis (this included 3 mice from the IL-10* group). Additionally, a mouse from the IL-10* group was also excluded as it showed a penile problem during testing, resulting in a final 13 mice for control and 11 mice for IL-10* for this test (Table S4).

QUANTIFICATION AND STATISTICAL ANALYSIS

For most experiments, control and treated mice or samples were processed in an alternate manner rather than in two large groups, to minimize batch effects. Although we did not do a bona fide power analysis, we took into account previous experiments to determine the number of animals needed for each type of experiments. Two-sided Wilcoxon rank sum test was used for comparison between specific groups, unless otherwise stated in figure legends. Statistical tests were performed in R (version 4.2.2) or in GraphPad Prism (version 10.2.0). Plots were generated in R ggplot2 (version 3.4.1) or Seurat (version 4.3.0) or GraphPad Prism. Results from individual experiments and statistical analysis are included in Table S4.